

# Fusion and decay dynamics of ${}^6\text{Li} + {}^{120}\text{Sn}$ and ${}^7\text{Li} + {}^{119}\text{Sn}$ reactions across the Coulomb barrier

Neha Grover,<sup>1,\*</sup> Ishita Sharma<sup>1b</sup>,<sup>2,†</sup> Manjeet Singh Gautam<sup>1c</sup>,<sup>3</sup> Manoj K. Sharma,<sup>4</sup> and P. K. Raina<sup>5</sup>

<sup>1</sup>*Department of Physics, School of Basic Sciences, Manipal University Jaipur, Jaipur, Rajasthan 303007, India*

<sup>2</sup>*Department of Physics, MCM DAV College for Women, Sector-36A, Chandigarh 160036, India*

<sup>3</sup>*Department of Physics, Government College Alewa, Jind-126102, Haryana, India*

<sup>4</sup>*School of Physics and Materials Science, Thapar Institute of Engineering and Technology, Patiala-147004, India*

<sup>5</sup>*Department of Physics, Indian Institute of Technology, Ropar, Rupnagar 140001, India*



(Received 17 March 2023; accepted 17 November 2023; published 21 December 2023)

In reference to the complete fusion (CF) and incomplete fusion (ICF) processes, the analysis of  ${}^6\text{Li} + {}^{120}\text{Sn}$  and  ${}^7\text{Li} + {}^{119}\text{Sn}$  reactions forming the  ${}^{126}\text{I}$  compound nucleus (CN) is carried out at incident energies spreading across the Coulomb barrier. The theoretical calculations of the formation of the compound nucleus  ${}^{126}\text{I}$  via two different entrance channels are done by opting for the energy-dependent Woods-Saxon potential (EDWSP) model and the  $\ell$ -summed Wong model. The available CF cross-section data of these systems at above-barrier energies is suppressed with respect to the EDWSP outcomes, and a reducing factor is needed to explain above-barrier CF data of given reactions. Such suppression effects at above-barrier energies can be correlated with the breakup of weakly bound systems ( ${}^{6,7}\text{Li}$ ) before reaching the Coulomb barrier. The total fusion (TF) cross-section data, which are the sum of CF and ICF cross-section data, are fairly addressed by using the EDWSP predictions. The difference between CF and TF data represents ICF yields and hence qualified in terms of range parameter  $r_0$ . Besides this, the  $\ell$ -summed Wong approach has been used to address CF, ICF, and TF cross-section data, which limits the contribution of partial waves to the maximum  $\ell$  value. Within the  $\ell$ -summed Wong model, the CF and ICF contributions are separated out on the basis of the angular-momentum window. In the angular-momentum distribution case, CF and ICF contributions are estimated in view of  $\ell$ -windows assigned for CF ( $\ell = 0$  to  $\ell_{\text{crit.}}$ ) and ICF ( $\ell_{\text{crit.}}$  to  $\ell_{\text{max}}$ ) components. Furthermore, the decay analysis of  ${}^{126}\text{I}$  compound nucleus is made using the dynamical cluster decay model (DCM). Calculations are made to analyze the decay cross sections  $\sigma_{xn}$  of neutron channels for given entrance channels at a wide spread of energies ( $E_{\text{lab}} = 14\text{--}28$  MeV). The neck-length parameter  $\Delta R$ , which decides the first turning point, is optimized to address the decay cross sections of different neutron evaporation channels and DCM-based calculations fairly explained the decay patterns of the CN.

DOI: [10.1103/PhysRevC.108.064607](https://doi.org/10.1103/PhysRevC.108.064607)

## I. INTRODUCTION

In recent years, an extensive experimental and theoretical effort have been made to understand the onset and reaction mechanisms induced by weakly bound nuclei such as  ${}^6,{}^7\text{Li}$ ,  ${}^9\text{Be}$ ,  ${}^{11}\text{Li}$  at low beam energies [1]. The weak binding energy and exotic structure of such projectiles is observed to have a strong influence on the fusion cross sections. As a consequence, there might be the suppression in the degree of fusion, which results in several other reaction mechanisms [2,3]. Therefore, reactions with these nuclei are of interest for probing the effect of low binding energy on fusion-fission and thus they open a new path to explore the exotic nuclear structure and associated reaction mechanisms. In this way, such reactions work as an application to observe different nuclear properties and thus in the production of different nuclear isotopes [4]

As a consequence of unusual features of weakly bound projectiles (WBPs), the essence of fusion reactions becomes

complex and leads to different reaction channels which can be classified on the basis of quantum of linear momentum transfer from the incident projectile to the target [5,6]. If there is direct and complete momentum transfer of beam to the target to form a compound nucleus, then the process is termed direct complete fusion (DCF), however, if the projectile breaks prior to amalgamation with the target, and all the broken clusters fuse with the target sequentially, then this process leads to sequential complete fusion (SCF). Both the SCF and DCF processes lead to the formation of the same compound nucleus with the same excitation energy and momentum transferred, making it difficult to differentiate between the two processes. Thus only the complete fusion (CF) cross section, which is the algebraic sum of SCF and DCF, can be observed experimentally [6]. Apart from the complete amalgamation of beam with target by different means (mentioned above), there might be an anticipation of incomplete momentum transfer or no momentum transfer process, where the former leads to incomplete fusion (ICF) and the latter process is termed noncapture breakup (NCBU) [1,4,6,7].

Partial momentum transfer in the fusion of  ${}^{197}\text{Au}$  and  ${}^{209}\text{Bi}$  targets with  ${}^{12}\text{C}$ ,  ${}^{14}\text{N}$ , and  ${}^{16}\text{O}$  beams at  $E_{\text{lab}} 7\text{--}10$  MeV/nucleon was first reported by Britt and Quinton [8].

\*Corresponding author: [nehagrover9823@gmail.com](mailto:nehagrover9823@gmail.com)

†Corresponding author: [ishitasharma2222@gmail.com](mailto:ishitasharma2222@gmail.com)

Since then, many approaches came forward to analyze weakly bound induced reactions. The foremost calculations of CF and ICF for loosely bound beams were based on classical mechanics, however, these calculations were not able to depict the tunneling effects [7,9–12]. Subsequently, various models and theories have been proposed to understand the influence of WBP on reaction mechanisms, such as in the breakup fusion model (BUF), the incident projectile is assumed to break up into its constituent clusters, e.g.,  ${}^9\text{Be}$  may break into  $\alpha + \alpha + 1n$ . Following the breakup, one of these fragments may fuse with the target nucleus to form the incompletely fused composite system, and the residue is emitted at forward angles with an energy  $E_{\text{residue}} = E_{\text{inc. Proj.}} A_{\text{residue}} / A_{\text{inc. Proj.}}$ .

Apart from above, few other methodologies such as Fermi jet models [13], are generally used to describe the fast-particle emission. Furthermore, the time-dependent Hartree–Fock model [14], Vlasov-Uehling-Uhlenbeck approach [15], continuum discretized coupled channel (CDCC) [12], moving source [16], hot-spot coalescence [17], spectator fragmentation [18] and other sophisticated methods based on quantum-mechanical approaches [19] have been examined and further improved [20–22] to understand the WBP induced reactions and thus ICF dynamics.

In heavy-ion collisions, the reaction mechanisms such as quasi-elastic processes, direct transfer of nucleons, cluster transfer and NCBU may compete with the ICF. All the processes mentioned above other than the ICF occur with much less dissipation of energy, however, in the case of ICF, there is a huge transfer of nucleons from projectile to target with a large dissipation of kinetic energy into the internal excitation of the colliding nuclei. Furthermore, ICF also depicts the process of transfer of a projectile component to the overlapping high-lying continuum states of the target, followed by the release of energetic nucleons. Also, in the case of ICF, there might be the emission of light charged particles and other channels such as  $\gamma$ ,  $\alpha$ , etc. due to the fact that, during breakup, WBP may release such particles prior to the fusion of ICF [23] or through deexcitation of the system formed via the ICF channel. To elaborate further, ICF includes the formation of intermediate composite nuclei (ICNs) via fusion of partial projectile or spectator component of the breakup channel [23]. Furthermore, this ICN may deexcite through particle evaporation, fission fragments,  $\gamma$  emission, etc.

In earlier investigations, a considerable number of studies (both experimental and theoretical) on ICF were performed at beam energies  $\approx 8$ – $10$  MeV/nucleon and the focus was mainly to detect the presence of ICF in strongly bound projectile-induced (SBP-induced) reactions. However, in recent years, ICF has been scrutinized extensively in reactions using WBP at energies around the Coulomb barrier (CB). It is noticed that, in WBP-induced reactions, there is strong suppression of CF cross sections in comparison with that of SBP-induced reactions. Furthermore, the analysis of competition between CF and ICF in HIRs is an efficacious tool to bring forth the information about the couplings due to breakup and transfer processes. Furthermore, it also depicts the effect of weak binding energies and the clustering nature of WBPs near barrier energies and thus may provide the particulars about the enhancement in breakup and transfer cross sections.

In view of the above, the present work mainly reports the theoretical investigation of WBP-induced reactions  ${}^6\text{Li} + {}^{120}\text{Sn}$  and  ${}^7\text{Li} + {}^{119}\text{Sn}$  [24], considering both fusion and decay processes. The calculations are made by using the EDWSP model [25–38],  $\ell$ -summed Wong [39–42], and dynamical cluster-decay model (DCM) [43–54]. The fusion dynamics of given reactions is analyzed within the ground work of the EDWSP model and the  $\ell$ -summed Wong model [39–42]. The decay analysis of compound nucleus formed in the aforementioned reactions is investigated by using the DCM formulation. The main objective of this work is to examine the effects of the breakup of WBP  ${}^6\text{Li}$  (and  ${}^7\text{Li}$ ) on fusion as well as on decay cross sections of chosen reactions at the given energy span ( $E_{\text{c.m.}} = 14$ – $26$  MeV). It has been found that the fusion and decay mechanism of weakly bound nuclei are quite different from that of fusion and decay process of stable systems. From decay point of view, the separation of CF and ICF process is also difficult because the emission of evaporation residue from these processes is very similar to reactions involving lighter mass targets. Upon interacting with heavier targets, the emission of alpha particles from the compound nucleus are generally used as a tool to separate two processes experimentally. The half time and characteristic energy of alpha nuclei are used to disentangle fusion of alpha and deuteron (ICF) from the complete fusion process [55,56]. The motive of the present study is to analyze the effects of the breakup of  ${}^6\text{Li}$  ( ${}^7\text{Li}$ ) projectile on the reaction dynamics involved with  ${}^{120}\text{Sn}$  ( ${}^{119}\text{Sn}$ ) target nucleus. Here, the target is a medium-mass nucleus having spherical shape due to proton shell closure at  $Z = 50$ .

In view of fusion dynamics, the CF cross-section data are found to be suppressed with respect to the EDWSP predictions particularly at above barrier energies. But the magnitude of suppression factor for both reactions turns out to be smaller than that of the reported values [24]. In literature [24], the complete fusion (CF) cross-section data are found to be suppressed by about 70% (85%) at above-barrier energies for the  ${}^6\text{Li} + {}^{120}\text{Sn}$  ( ${}^7\text{Li} + {}^{119}\text{Sn}$ ) reaction when compared with the universal fusion function as standard reference. However, the EDWSP model [25–38] estimates the CF suppression at above barrier for  ${}^6\text{Li} + {}^{120}\text{Sn}$  ( ${}^7\text{Li} + {}^{119}\text{Sn}$ ) reaction by 82% (90%) while the subbarrier fusion data are fairly reproduced by the EDWSP model. In this sense within the EDWSP approach, the above barrier CF suppression factor for  ${}^6\text{Li} + {}^{120}\text{Sn}$  ( ${}^7\text{Li} + {}^{119}\text{Sn}$ ) reaction can be minimized by 12% (5%) when compared with the results reported in Ref. [24] and EDWSP suppression factors are noticeably smaller than that of the reported values. This suppression appeared due to the breakup of loosely bound projectile in the force field of target prior to the Coulomb barrier and suppression effects can be correlated with the breakup threshold of the weakly bound system. The breakup threshold of lighter projectile ( ${}^6\text{Li}$ ) is 1.475 MeV, is much lower than the breakup threshold (2.45 MeV) of the heavier projectile ( ${}^7\text{Li}$ ). Therefore, the larger suppression factor is expected for the lighter projectile and hence the same is evident from the EDWSP predictions. On the other hand, the TF cross-section data, which is the sum of CF and ICF cross-section data, are properly addressed by the EDWSP outcomes.

To strengthen the above conclusions, the fusion dynamics of the studied reactions is also analyzed within the view of the  $\ell$ -summed Wong model. The Wong formula [57] could not address CF and TF cross-section data simultaneously for the given reactions (works only for TF cross sections). Therefore,  $\ell$ -summed Wong model is used to predict the complete and incomplete fusion excitation function. The  $\ell$ -summed Wong model is able to distinguish the contribution of the CF and ICF processes along with TF on the basis of angular-momentum values. These values are calculated using the sharp cut of approximation [6,39]. The results obtained find good agreement with the experimentally measured CF, ICF, and TF cross sections for both  ${}^6,7\text{Li}$ -induced reactions. To get further insight regarding the role of projectile breakup effects, the decay mechanism of the same reactions is elaborated within the framework of DCM. The main components of DCM from which important information about the decay can be obtained include the fragmentation potential, preformation probability, and barrier modification. The breakup process has eminent effect on the decay process as the compound systems formed via CF and ICF channels are different [24]. According to the experimental study, the  ${}^6\text{Li}$  ( ${}^7\text{Li}$ ) breaks into  ${}^4\text{He}$  and  ${}^2\text{H}$  ( ${}^3\text{H}$ ) and the probability of fusion of  ${}^2\text{H}$  ( ${}^3\text{H}$ ) with  ${}^{120}\text{Sn}$  ( ${}^{119}\text{Sn}$ ) is expected to be large, accordingly. Therefore, the decay analysis of  ${}^{126}\text{I}$  (formed in CF) and  ${}^{122}\text{Sb}$  (formed in ICF) has been examined. Both CF and ICF cross sections are addressed at the given energy range.

The organization of this paper is as follows: A brief account of the theoretical formalisms is presented in Section II. The calculations and results for excitation functions of both CF and ICF processes (in view of both fusion and decay channels) are discussed in Sec. III. Finally, the results are summarized in Sec. IV.

## II. THEORETICAL FORMALISM

In this section, formalisms used to pursue the calculations are discussed. To explain all methodologies clearly, this section is divided into three sections. Section II A defines the EDWSP model. Section II B explains the  $\ell$ -summed Wong model, and Sec. II C describes the dynamical cluster-decay model.

### A. Energy-dependent Woods-Saxon potential model

Within the view of partial-wave analysis, the total fusion cross sections are given by

$$\sigma_F = \frac{\pi}{k^2} \sum_{\ell} (2\ell + 1) T_{\ell}^F, \quad (1)$$

$$V_0 = \left[ (A_P^{2/3} + A_T^{2/3}) - (A_P + A_T)^{2/3} \right] \left[ 2.38 + 6.8(1 + I_P + I_T) \frac{A_P^{1/3} A_T^{1/3}}{(A_P^{1/3} + A_T^{1/3})} \right] \text{MeV}, \quad (6)$$

where  $I_P = (N_P - Z_P)/A_P$  and  $I_T = (N_T - Z_T)/A_T$  are the isospin asymmetry of the participating systems. This parametrization has been extracted by reproducing the fusion data of many projectile-target combinations ranging from  $Z_P Z_T = 84$  to  $Z_P Z_T = 1640$ . In the EDWSP approach, the energy dependence in the Woods-Saxon potential is taken via its diffuseness parameter,

where  $k = (\frac{2\mu E_{c.m.}}{\hbar^2})^{1/2}$ ,  $\ell$  is the partial-wave number, and  $T_{\ell}^F$  is the transmission probability for the  $\ell$ th partial wave.

Hill and Wheeler [57] based on parabolic approximation suggested a simple formula for estimating the tunneling probability. In this approximation, the effective interaction potential between the heavy ions has been replaced by an inverted parabola and the tunneling probability ( $T_{\ell}^{HF}$ ), which is defined as

$$T_{\ell}^{HW} = \frac{1}{\left[ 1 + \exp \frac{2\pi}{\hbar\omega_{\ell}} (V_{\ell} - E_{c.m.}) \right]}. \quad (2)$$

$V_{\ell}$  and  $\hbar\omega_{\ell}$  used in above equation is the total interaction potential and barrier curvature, respectively, for the  $\ell$ th partial wave. By replacing the expression of transmission probability  $T_{\ell}^F$  by the Hill-Wheeler expression of transmission probability  $T_{\ell}^{HW}$ , one can calculate the total fusion cross sections corresponding to each partial wave, and this parabolic approach is known as the Hill-Wheeler approximation.

This parabolic approximation was further modified by Wong using the assumptions for barrier position, barrier curvature, and barrier height [58] and obtained the simple formula for evaluation of fusion cross sections which is given by the following relation:

$$\sigma^F(E_{c.m.}) = \frac{\hbar\omega R_B^2}{2E_{c.m.}} \ln \left[ 1 + \exp \frac{2\pi}{\hbar\omega} (E_{c.m.} - V_{B0}) \right], \quad (3)$$

where  $V_{B0}$  is height of the Coulomb barrier.  $R_B$  and  $\hbar\omega$  are the barrier position and barrier curvature for the Coulomb barrier, respectively.

For the theoretical description, the nucleus-nucleus potential is the most sensitive input and can modify the theoretical predictions. Therefore, it is essential to use an appropriate form of the nucleus-nucleus potential to analyze the experimental data. In recent works, the EDWSP model [25–38] has been successfully applied to preview the dynamics of heavy ion fusion reactions. The form of the static Woods-Saxon potential is defined as

$$V_N(r) = \frac{-V_0}{\left[ 1 + \exp \left( \frac{R-R_0}{a} \right) \right]}, \quad (4)$$

with

$$R_0 = r_0(A_P^{1/3} + A_T^{1/3}). \quad (5)$$

The quantity  $V_0$  is the depth and  $a$  is the diffuseness parameter of the nuclear potential. In the EDWSP approach, the depth of the real part of the Woods-Saxon potential is obtained by using the following parametrization:

which is defined as

$$a(E) = 0.85 \left[ 1 + \frac{r_0}{13.75(A_P^{-1/3} + A_T^{-1/3}) \left[ 1 + \exp\left(\frac{E_{c.m.}/V_{B0} - 0.96}{0.03}\right) \right]} \right] \text{fm.} \quad (7)$$

Equation (7) is extracted by using the sigmoidal fitting of the reproduction of the fusion data of various nuclear reactions. In fusion dynamics, the numerous physical effects which can directly or indirectly influence the mechanism of quantum tunneling through the fusion barrier are variations of the  $N/Z$  ratio, surface energy, and surface diffuseness of the colliding pairs, dynamical density evolutions, change of density profile of the collision partners in the neck region, and dissipation of kinetic energy of relative motion to internal excitations during formation of the compound nuclei. The above-mentioned physical effects also affect the radial dependence of the nucleus-nucleus potential during nuclear interactions and consequently modify the potential parameters. As a result, the different sets of the potential parameters are used to explore the different types of nuclear interactions. In the literature, it was pointed out that the energy dependence in the nucleus-nucleus potential originates from effective nucleon-nucleon interactions and the nonlocal quantum effects and hence is the most essential feature of the nuclear potential [59]. These physical effects involve the exchange of nucleons between the colliding systems and consequently generate an energy dependence in the nuclear potential. The energy dependence in the nucleus-nucleus potential can also originate from the coordinate-dependent mass and channel coupling effects, and such effects are clearly reflected from the microscopic time-dependent Hartree-Fock theory [60–62]. To include all the aforementioned physical effects, the EDWSP model, wherein the energy dependence in the Woods-Saxon potential is considered through its diffuseness parameter, was proposed.

In the EDWSP model, the value of the range parameter  $r_0$  can be correlated with the geometrical shape and density evolutions of the fusing nuclei along fusion path. The range of the diffuseness parameter, which is required for addressing the observed fusion dynamics of the colliding nuclei under consideration, also depends on the range parameter  $r_0$  through Eq. (7). In this regard, the different set of values of the range parameter are required to describe the dynamics of the different fusing pairs which in turn geometrical defines the radii of the fusing nuclei [ $R_0 = r_0(A_P^{1/3} + A_T^{1/3})$ ] as done in the usual coupled-channel approach [56,63–65]. The potential depth  $V_0$  can be determined by using Eq. (6). As already mentioned, the value of diffuseness parameter and range parameter  $r_0$  of the EDWSP model are mathematically related with each other via Eq. (7), and the change in range parameter intrinsically produces corresponding adjustments in the values of diffuseness parameter and, subsequently, the values of barrier characteristics associated with the Coulomb barrier. Therefore, the variations in the diffuseness parameter is directly associated with the dynamical evolution of density profile of the collision partners that subsequently reflects this dynamical change of geometrical shape of the collision partners along the fusion path. In the coupled-channel

approach, the inclusion of different intrinsic channels associated with reactants imparts barrier modifications and such barrier modifications appear in the form of the fluctuation of radii of colliding nuclei. In a similar way, the energy dependence in Woods-Saxon potential results in barrier modifications by bringing dynamical evolution of the density profile of the collision partners that ultimately leads to the dynamical change of geometrical shape of the colliding nuclei during fusion process. In the EDWSP model, such dynamical changes in the geometrical shape are interpreted in terms of fluctuation of radii of the fusing partners. Thus, the EDWSP calculations are done by taking the parameters as defined by Eqs. (4)–(7) into Eq. (3) with  $V_{B0}$  replaced by the EDWSP barrier height. The EDWSP barrier height is defined as

$$V_{B0}^{\text{EDWSP}} = V_N(r = r_B) + V_C(r = r_B), \quad (8)$$

$$V_{B0}^{\text{EDWSP}} = \frac{-V_0}{\left[ 1 + \exp\left(\frac{R_B - R_0}{a(r)}\right) \right]} + \frac{Z_P Z_T e^2}{R_B}. \quad (9)$$

### B. $\ell$ -summed Wong model

In the  $\ell$ -summed Wong model, the Wong formula [57,58] is extended for summation over  $\ell$  and fusion cross sections are calculated for each partial wave. In this model, the tunneling probability due to Hill and Wheeler as defined in Eq. (2) is taken as a function of  $\ell$ , orientation angle ( $\theta_i$ ,  $i = 1, 2$ ) and deformations, and hence is given by Eq. (2), explained in the previous section. For details see Refs. [39–42].

The temperature dependence in each potential is introduced via the radius vectors of two nuclei that reads

$$R_i(\alpha_i, T) = R_{0i}(T) \left[ 1 + \sum_{\lambda} \beta_{\lambda i} Y_{\lambda}^{(0)}(\alpha_i) \right], \quad (10)$$

where the  $T$ -dependent nuclear radii  $R_{0i}(T)$  of the equivalent spherical nuclei [66] is

$$R_{0i}(T) = [1.28A_i^{1/3} - 0.76 + 0.8A_i^{-1/3}](1 + 0.0007T^2). \quad (11)$$

Within the  $\ell$ -summed Wong model, the Hill-Wheeler tunneling probability  $T_{\ell}^{\text{HW}}$  is calculated in terms of barrier curvature  $\hbar\omega_{\ell}$  and barrier height  $V_B^{\ell}$ , for each partial wave. Using Eq. (2) into Eq. (1), the fusion cross sections become

$$\sigma(E_{c.m.}, \theta_i) = \frac{\pi}{k^2} \sum_{\ell=0}^{\ell_{\max}} (2\ell + 1) T_{\ell}^{\text{HW}}(E_{c.m.}, \theta_i). \quad (12)$$

In the extended version of the Wong formula [39–42], the summation over  $\ell$  partial wave is limited up to the angular momentum window that varies from angular momentum  $\ell = 0$  to the  $\ell = \ell_{\max}$  value. The maximum above-barrier angular momentum is obtained using the sharp cutoff approximation

[6,39], which is given as

$$\ell_{\max} = R_B \sqrt{2\mu(E_{c.m.} - V_B)/\hbar^2}. \quad (13)$$

Since the sharp cutoff model is only applicable to above-barrier energies, an energy-dependent interpolation is used to estimate the  $\ell$  values at below-barrier energies. Furthermore, by making use of above-mentioned  $\ell_{\max}$  values, the critical  $\ell$  values are determined by using the approach mentioned in Refs. [5,6] with the experimental [24] cross sections as an input. Subsequently, theoretical cross sections are calculated by using these  $\ell_{\text{crit}}$  values in the  $\ell$ -summed Wong model as

$$\sigma_{CN}(E_{c.m.}, \theta_i) = \frac{\pi}{k^2} \sum_{\ell=0}^{\ell_{\text{crit}}} (2\ell + 1) T_{\ell}^{\text{HW}}(E_{c.m.}, \theta_i). \quad (14)$$

Above the critical  $\ell$  values, the contribution of the ICF process tends to increase, therefore the cross section of the incomplete fusion process takes place for  $\ell$  values lies in the limit  $\ell_{\text{crit}} < \ell < \ell_{\max}$  [67] and is given as

$$\sigma_{\text{ICF}}(E_{c.m.}, \theta_i) = \frac{\pi}{k^2} \sum_{\ell=\ell_{\text{crit}}}^{\ell_{\max}} (2\ell + 1) T_{\ell}^{\text{HW}}(E_{c.m.}, \theta_i). \quad (15)$$

Finally, the total fusion cross sections are expressed as the sum  $\sigma_{\text{TF}} = \sigma_{\text{CF}} + \sigma_{\text{ICF}}$  or

$$\sigma_{\text{TF}}(E_{c.m.}, \theta_i) = \frac{\pi}{k^2} \sum_{\ell=0}^{\ell_{\max}} (2\ell + 1) T_{\ell}^{\text{HW}}(E_{c.m.}, \theta_i). \quad (16)$$

After the fusion process explained in Secs. II A and II B, the decay dynamics is explained in the subsequent section.

### C. The dynamical cluster-decay model

The DCM [43–54] deals with various decay modes such as evaporation residue (ER), intermediate mass fragments (IMFs), heavy-mass fragments (HMFs), and fission. Here, we use the collective coordinates of mass (and charge) asymmetries  $\eta_A = (A_1 - A_2)/(A_1 + A_2)$  [and  $\eta_Z = (Z_1 - Z_2)/(Z_1 + Z_2)$ ]; 1 and 2 stand, respectively, for heavy and light fragments], the relative separation  $R$ , which includes the multipole deformations  $\beta_{\lambda i}$  ( $\lambda = 2, 3, 4$ ) and orientations  $\theta_i$  ( $i = 1, 2$ ) of two nuclei or fragments. In the DCM formalism, to investigate the compound nucleus decay, the preformation probability  $P_0$  refereing to  $\eta$  [ $= A_1 A_2 / (A_1 + A_2)$ ] motion is an essential factor to attain the information related to preborn fragments in the CN system. The DCM found its origin in the quantum-mechanical fragmentation theory (QMFT) [52–54], and the decay cross sections in DCM are calculated as

$$\sigma = \frac{\pi}{k^2} \sum_{\ell=0}^{\ell_{\max}^{\text{DCM}}} (2\ell + 1) P_0 P, \quad k = \sqrt{\frac{2\mu E_{c.m.}}{\hbar^2}}. \quad (17)$$

Here, the maximum angular momentum  $\ell_{\max}^{\text{DCM}}$  mentioned in the above equation is defined [43–54] as the maximum  $\ell$  value for the light particle evaporation residue cross section  $\sigma_{ER}$ , where  $\sigma_{ER} \rightarrow 0$ . Furthermore, the decay cross sections in the DCM are calculated by using decoupled approximations to  $R$  and  $\eta$  motion and the Schrödinger wave equation in  $\eta$

coordinates reads

$$\left[ -\frac{\hbar^2}{2\sqrt{B_{\eta\eta}}} \frac{\partial}{\partial \eta} \frac{1}{\sqrt{B_{\eta\eta}}} \frac{\partial}{\partial \eta} + V_R(\eta, T) \right] \psi^v(\eta) = E_{\eta}^v \psi^v(\eta). \quad (18)$$

Here,  $B_{\eta\eta}$  is a smooth hydrodynamical mass parameter [68] and  $v = 0, 1, 2, 3, \dots$  refers to the ground state ( $v = 0$ ). The solution of Eq. (18) gives the preformation probability  $P_0$  and is defined by the following equation:

$$P_0 = |\psi(\eta(A_i))|^2 \sqrt{B_{\eta\eta}} \frac{2}{A_{CN}}, \quad (19)$$

where  $A_{CN}$  is the mass of the compound nucleus. The structural information analyzed via the preformation probability  $P_0$  enters through the fragmentation potential, which is defined as

$$\begin{aligned} V_R(\eta, T) = & \sum_{i=1}^2 [V_{LDM}(A_i, Z_i, T)] + \sum_{i=1}^2 [\delta U_i] \exp(-T^2/T_0^2) \\ & + V_C(R, Z_i, \beta_{\lambda i}, \theta_i, T) + V_P(R, A_i, \beta_{\lambda i}, \theta_i, T) \\ & + V_{\ell}(R, A_i, \beta_{\lambda i}, \theta_i, T). \end{aligned} \quad (20)$$

At each temperature  $T$ , the fragmentation potential  $[V_R(\eta, T)]$  is calculated by using the Strutinsky macro-microscopic method, where the macroscopic term  $V_{LDM}$  is the  $T$ -dependent liquid drop energy of Davidson *et al.* [69], with its constants at  $T = 0$  refitted [70] to give the experimental binding energies [71]. The microscopic shell corrections  $\delta U$  are calculated using estimates of Myers and Swiatecki [72].  $V_C$ ,  $V_P$ , and  $V_{\ell}$  are, respectively, the  $T$ -dependent, Coulomb, nuclear proximity, and the angular-momentum-dependent potentials for deformed nuclei with the moment of inertia taken in the complete sticking limit.

The tunneling or penetration probability  $P$  used in Eq. (17) refers to  $R$  motion and is calculated by using the WKB approximation as

$$P = \exp \left[ -\frac{2}{\hbar} \int_{R_a}^{R_b} \{2\mu[V(R) - Q_{\text{eff}}]\}^{1/2} dR \right]. \quad (21)$$

The above equation is solved analytically [73,74], where  $V(R)$  is the sum of  $V_P$ ,  $V_C$ , and  $V_{\ell}$  satisfying the condition  $V(R_a) = V(R_b) = Q_{\text{eff}}$ , with  $R_b$  as exit point and  $R_a$  as entry point of barrier penetration and defined as  $R_a = R_1(\alpha, T) + R_2(\alpha, T) + \Delta R(T)$ .  $\Delta R$  is the separation distance between the surfaces of two fragments, known to assimilate the neck-formation effects, and hence referred to as the neck-length parameter. This inclusion of the neck-length parameter leads to corresponding barrier modification, which is defined as

$$\Delta V_B(\ell) = V(R_a, \ell) - V_B(\ell). \quad (22)$$

Within the DCM model, the disentanglement the CF and ICF processes is carried out on the basis of the beam energy of the WBPs. Subsequent to the breakup of a WBP, there is a formation of two different compound nuclei due to the CF and ICF channels. The particle emission from both the CF and ICF decay path is different. Assuming that the velocity of the spectator fragment (part of the projectile which does not fuse with the target after breakup), the damping in energy due to

the fractional energy carried away by the spectator after the breakup is expressed as

$$E_S = E_1 * A^S. \quad (23)$$

In above equation,  $A^S$  symbolizes the mass of the spectator and  $E_1 = E_{\text{beam}}/A_{\text{WBP}}$  is the energy per nucleon with  $A_{\text{WBP}}$  being the mass of the projectile before breakup, i.e., of  ${}^6\text{Li}$  (projectiles in the present work). Therefore, the energy of remnant part of the projectile, which hits the target in the ICF, is

$$E_{RP}^{\text{ICF}} = E_{\text{beam}} - E_S. \quad (24)$$

### III. RESULTS AND DISCUSSION

Following the importance of WBP-induced reactions, as discussed in Sec. I, a detailed description of the dynamics of reactions with reactions induced by the weakly bound projectiles  ${}^6\text{Li}$  and  ${}^7\text{Li}$  is presented here. The fusion dynamics as well as decay mechanism of the  ${}^{126}\text{I}$  compound system formed via two entrance channels such as  ${}^6\text{Li} + {}^{120}\text{Sn}$  and  ${}^7\text{Li} + {}^{119}\text{Sn}$  having same Coulomb factor  $Z_1Z_2 = 150$  is studied around the Coulomb barrier energies. The fusion process is analyzed in view of the EDWSP model and the  $\ell$ -summed Wong formalism. In the EDWSP model, the energy-dependent nature of the Woods-Saxon potential governs barrier modifications and the distinction between the CF, ICF, and TF cross sections are interpreted in terms of the range parameter  $r_0$ . In the  $\ell$ -summed Wong formalism, wherein deformation and orientation effects are taken into consideration, the distinction between complete fusion (CF) from incomplete fusion (ICF) processes are done on the basis of angular momentum  $\ell$  values. In addition to this, the decay of compound systems formed by CF and ICF channels is also analyzed by using the DCM. Here, CF and ICF is differentiated on the basis of energy loss of the projectile. To demonstrate the results in a better way, the present section is divided into two sections. Section III A deals with the study of the fusion process and, in Sec. III B, the decay profile of compound systems formed via the CF and ICF channels is discussed in view of the DCM formalism.

#### A. Fusion dynamics

##### 1. Fusion dynamics by using the EDWSP model

In Fig. 1, the variable energy-dependent fusion barriers at different incident energies are shown as a function of radial separation for the  ${}^6\text{Li} + {}^{120}\text{Sn}$  reaction, and the similar results are turned out for  ${}^7\text{Li} + {}^{119}\text{Sn}$  reaction. Due to the energy dependence in the Woods-Saxon potential, the attractive nature of the EDWSP increases at near and subbarrier energies. Such an enhanced attractive nature of the EDWSP governs gross-potential modifications and subsequently modifies the barrier profile and barrier characteristics in such a way that effective fusion barrier between participants decreases. In other words, the EDWSP model brings splitting of the single interaction barrier into a set of energy-dependent fusion barriers of different heights. In this spectrum of energy-dependent fusion barriers, the height of one and/or more barriers is smaller than that of the Coulomb barrier and allows the passage of

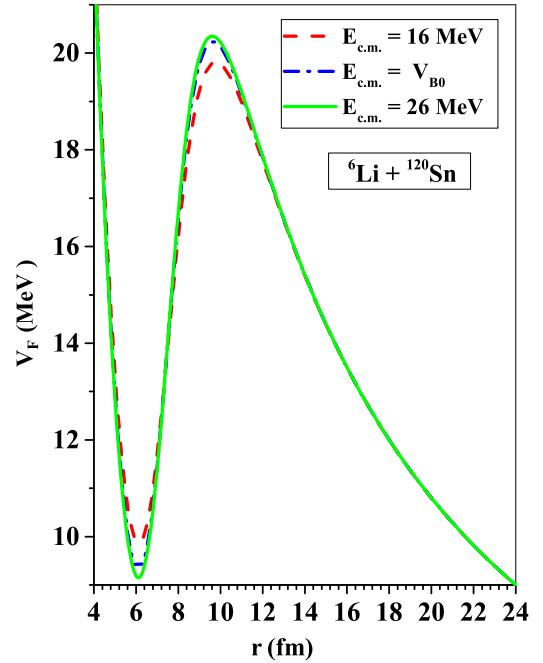


FIG. 1. The EDWSP fusion barrier (FB) as a function of relative separation  $r$  (fm) at different incident energies in the center-of-mass frame ( $E_{\text{c.m.}}$ ) for the  ${}^6\text{Li} + {}^{120}\text{Sn}$  reaction. Similar results are found for the  ${}^7\text{Li} + {}^{119}\text{Sn}$  reaction (not shown here to avoid repetition).

the flux from the entrance channel to fusion and/or other reaction channels. Thus, the EDWSP distributes the incoming flux into the fusion channel and, consequently, the model calculations predict a larger fusion excitation function when compared with the outputs of a one-dimensional barrier penetration model (BPM). Similar results are also evident from the usual coupled-channel calculations, as done by the authors of Ref. [24], wherein the couplings to low-lying quantum states or static deformations and/or the particle transfer channel are done with the relative separation coordinates of the fusing partners [24]. Similar results are found for the  ${}^7\text{Li} + {}^{119}\text{Sn}$  reaction. Hence, the barrier lowering produced in the EDWSP model make it an efficient tool to describe subbarrier fusion anomalies for given reactions. For the  ${}^6\text{Li} + {}^{120}\text{Sn}$  ( ${}^7\text{Li} + {}^{119}\text{Sn}$ ) reaction, the largest diffuseness produced is  $a = 0.939$  fm ( $a = 0.941$  fm for  ${}^7\text{Li} + {}^{119}\text{Sn}$ ), which in turn leads to the lowest energy-dependent fusion barrier (FB). This ultimately brings the shifting of the elastic flux from the entrance channel to the fusion channel and subsequently enhances the magnitude of the fusion cross sections at energies below the Coulomb barrier.

In this model, the diffuseness parameter depends on incident energy, and the diffuseness parameter decreases as the incident energy increases (see Table I). For the  ${}^6\text{Li} + {}^{120}\text{Sn}$  ( ${}^7\text{Li} + {}^{119}\text{Sn}$ ) reaction, as the incident energy increases from 14 MeV to 28 MeV, the diffuseness decreases from  $a = 0.939$  fm to  $a = 0.850$  fm ( $a = 0.941$  fm to  $a = 0.850$  fm). Such variation in diffuseness subsequently modifies the height of the energy-dependent fusion barrier (EDFB) from EDFB = 19.695 MeV to EDFB = 20.093 MeV (EDFB = 19.251 MeV to EDFB = 19.710 MeV; see Fig. 1). The difference between

TABLE I. Range, depth, and diffuseness of the Woods-Saxon potential used in EDWSP model calculations for the chosen reactions.

System	$r_0$ (fm)	$V_0$ (MeV)	$\frac{a^{\text{Present}}}{\text{Energy range}} \left( \frac{\text{fm}}{\text{MeV}} \right)$	Reference
${}^6\text{Li} + {}^{120}\text{Sn}$	1.090	32.25	$\frac{(0.939) \text{ to } (0.850)}{(14) \text{ to } (28)}$	[24–38]
${}^7\text{Li} + {}^{119}\text{Sn}$	1.080	39.64	$\frac{(0.941) \text{ to } (0.850)}{(14) \text{ to } (28)}$	[24–38]

such lowest energy-dependent fusion barrier and the corresponding Coulomb barrier ( $V_{B0} = 19.740$  MeV as given in Table II) is 0.045 MeV. This in turn suggests that the barrier modification is required to explain the fusion data of the present reaction at subbarrier energies. At below-barrier-energy regions, the distribution of energy-dependent fusion barriers suggest that there is a strong influence of nuclear structure degrees of freedom on the fusion data. At well above the Coulomb barrier, the saturation of diffuseness to its minimum value ( $a = 0.85$  fm) ceases the change in the height of energy-dependent fusion barrier (EDFB) and results in the saturation of the experimental data. Similar results as evident from Fig. 1 are applicable for the  ${}^7\text{Li} + {}^{119}\text{Sn}$  reaction as well.

The results of the EDWSP calculations for the CF and TF cross sections of the studied systems are shown in Figs. 2 and 3. In Fig. 2, the CF cross sections estimated by using the EDWSP model are compared with available experimental data. Theoretical calculations performed by Eqs. (10) and (11)

TABLE II. The values of  $V_{B0}$ ,  $R_B$ , and  $\hbar\omega$  used in the EDWSP model calculations for the studied reactions.

System	$V_{B0}$ (MeV)	$R_B$ (fm)	$\hbar\omega$ (MeV)	Reference
${}^6\text{Li} + {}^{120}\text{Sn}$	19.740	10.18	4.16	[24]
${}^7\text{Li} + {}^{119}\text{Sn}$	19.480	10.34	3.82	[24]

of Ref. [24] are also compared with the EDWSP predictions. EDWSP calculations find nice resemblance with referred data, which confirms the validity and predictive power of the EDWSP model. As already mentioned, the energy-dependent nature of Woods-Saxon potential governs the attractive interaction for the projectile and target system. As a result, the effective fusion barrier between the participants gets reduced in comparison with the uncoupled Coulomb barrier  $V_{B0}$  and, consequently, the EDWSP model predicts larger fusion cross sections over the outcomes of the BPM. The EDWSP predictions empirically include the impact of dominant channel couplings, and the predictions made via the coupled-channel approach and the EDWSP method closely resemble in the near and subbarrier energy regimes, as evident from earlier works [25–38]. In essence of barrier lowerings, the EDWSP model reasonably reproduces subbarrier CF cross-section data but the same calculations overpredict the CF fusion data at above-barrier energies for both reactions.

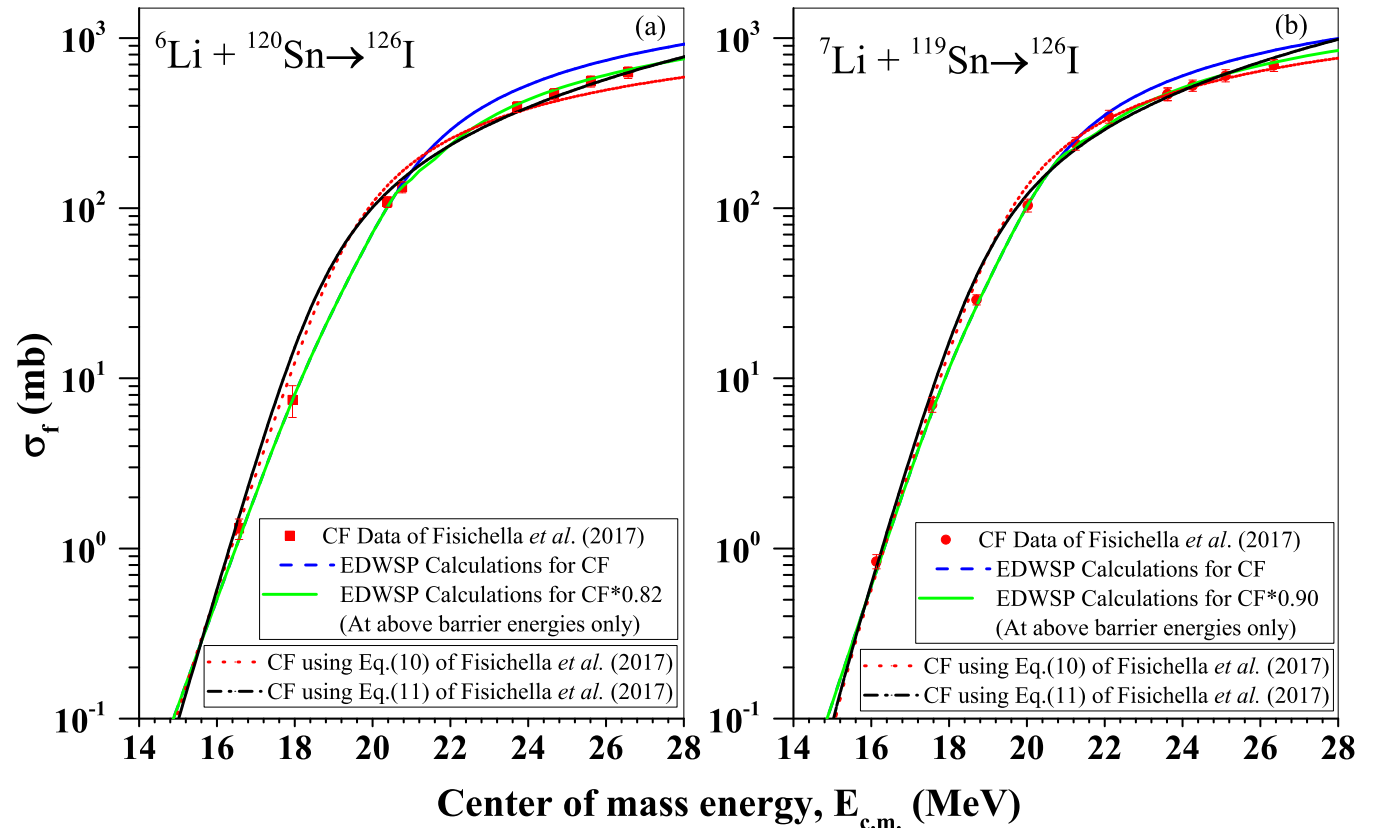


FIG. 2. The CF excitation function of (a)  ${}^6\text{Li} + {}^{120}\text{Sn}$  and (b)  ${}^7\text{Li} + {}^{119}\text{Sn}$  reactions obtained using the EDWSP model. The results are compared with the available experimental data taken from Fichella *et al.* (2017) [24].

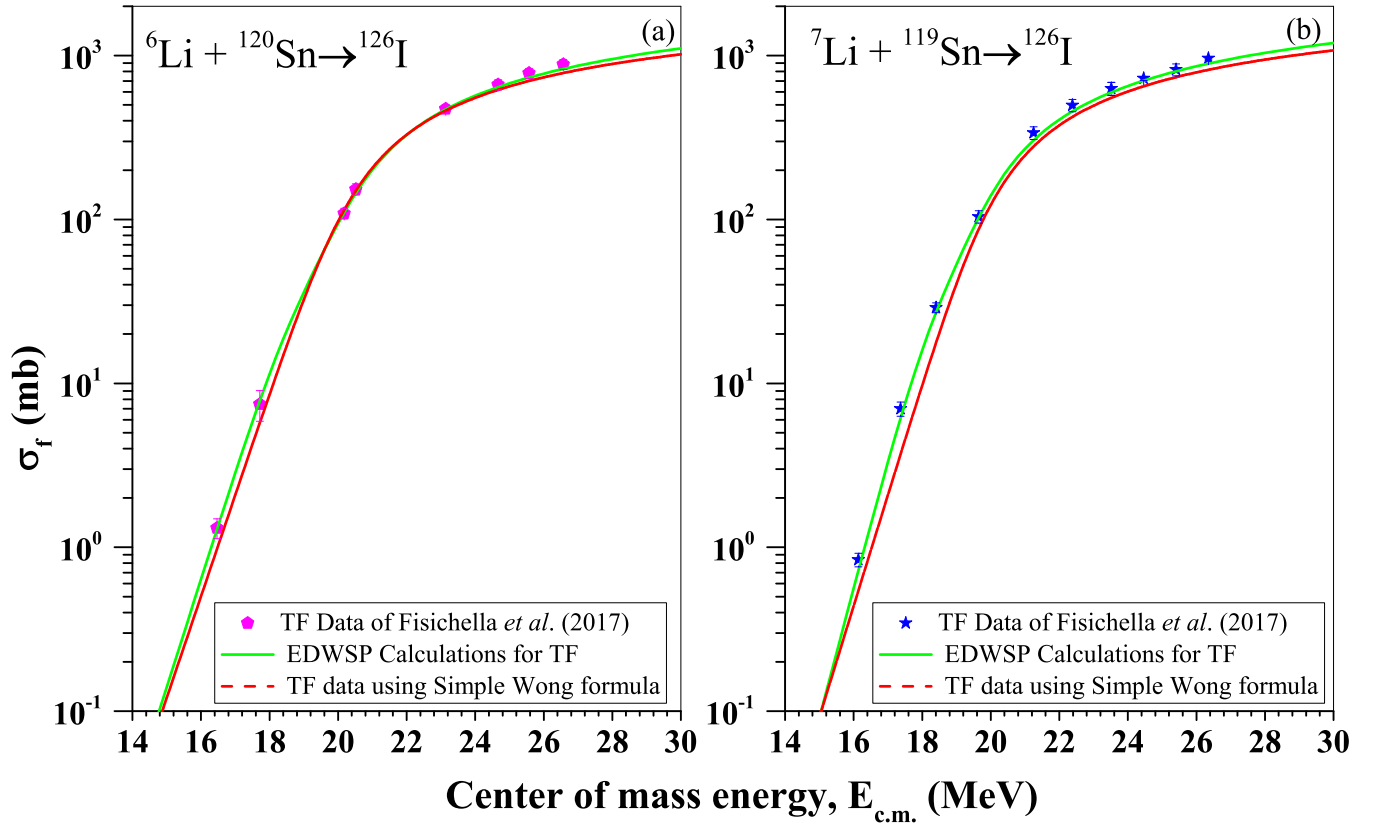


FIG. 3. The TF excitation function of the  ${}^6\text{Li} + {}^{120}\text{Sn}$  and  ${}^7\text{Li} + {}^{119}\text{Sn}$  reactions obtained using the EDWSP model [25,28,29]. The results are compared with the available experimental data of Fisichella *et al.* (2017) [24].

For the  ${}^6\text{Li} + {}^{120}\text{Sn}$  reaction, CF cross sections at the subbarrier domain are properly addressed by EDWSP calculations for a range parameter  $r_0 = 1.090$  fm, which indicates that all the dominant channel couplings are empirically included in the EDWSP-based results. However, this calculation overestimates the CF cross-section data at above-barrier energies by 18% [see Fig. 2(a)]. In Ref. [24], the authors suggested that the fusion suppression factor for the  ${}^6\text{Li} + {}^{120}\text{Sn}$  reaction is approximately 30% when compared with the universal fusion function as a standard reference. The EDWSP estimations suggest that the above-barrier CF cross-section data for given reaction are suppressed by 18% and such a suppression factor is appreciably smaller than that of the reported value. For the  ${}^7\text{Li} + {}^{119}\text{Sn}$  reaction, the CF cross sections in subbarrier energy regimes are explained within the preview of the EDWSP model with range parameter  $r_0 = 1.080$  fm and such a calculation also incorporates the possible impact of the internal structure degrees of freedom associated with the collision partners. This range parameter is sufficient to drive the relevant channel couplings in the subbarrier energy region during the fusion process. But the so-obtained calculation overpredicts the CF cross-section data at above-barrier energy regions by 10% [see Fig. 2(b)], which is again lower than the suppression factor reported in literature [24]. Thus, the EDWSP suppression factor for the  ${}^6\text{Li} + {}^{120}\text{Sn}$  ( ${}^7\text{Li} + {}^{119}\text{Sn}$ ) reaction can be minimized up to 12% (5%) with reference to the reported values. For both reactions, the CF cross-section data at above-barrier energies are inhibited with

respect to the EDWSP predictions but the magnitude of the suppression factors is sufficiently smaller than that of the reported values in the literature. The predictions of Eqs. (10) and (11) of Ref. [24] are compared with the EDWSP predictions. The EDWSP predictions are in close agreement with the data [24] at subbarrier energies but, at above-barrier energies, the EDWSP predictions needed a reduction factor to explain the CF cross sections of both reactions. There is also an overall agreement between the predictions of CF using Eqs. (10) and (11) of Ref. [24]. The suppression of above-barrier CF data for both studied systems appeared due to the loosely bound nature of the projectile. As a result of low breakup thresholds, the weakly bound projectile breaks up into two parts as  ${}^6\text{Li} \rightarrow \alpha + d$  ( ${}^7\text{Li} \rightarrow \alpha + t$ ) and hence the projectile is partially absorbed by the target. In this regard, the fusion yields get reduced at above-barrier energies and such effects are more pronounced as the breakup threshold decreases. Thus, the EDWSP suppression factor for the  ${}^6\text{Li}$ -induced reaction is smaller than that of the  ${}^7\text{Li}$ -induced reaction, which can be correlated with the lower breakup threshold of the lighter projectile ( ${}^6\text{Li}$ ) in comparison with that of the heavier projectile ( ${}^7\text{Li}$ ). Similar conclusions are also evident from Ref. [24]. Thus, the presence of ICF yields clearly reflects the breakup of the loosely bound system prior to the Coulomb barrier and hence the same is also evident from the present work.

The total fusion (TF) cross-section data, which are sum of CF and ICF cross-section data, are fairly addressed by EDWSP-based calculations for both systems, as depicted in

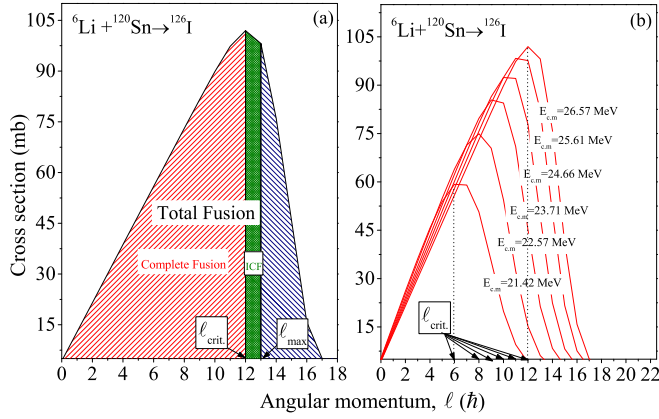


FIG. 4. (a) Angular-momentum distribution of different reaction processes obtained for the  ${}^6\text{Li} + {}^{120}\text{Sn}$  channel using the  $\ell$ -summed Wong formula at  $E_{c.m.} = 26.7$  MeV and (b) Variation in the  $\ell_{crit.}$  values studied with respect to incident energy  $E_{c.m.}$ .

Fig. 3. Comparative analysis of TF calculated using EDWSP model and the simple Wong formula is depicted in Fig. 3. It is clearly visible from the figure that cross sections calculated using the simple Wong formula are slightly deviated with respect to the TF data, however, the EDWSP explains the TF cross section in a nice manner. To explain the TF cross-section data, the chosen value of the range parameter is  $r_0 = 1.120$  fm ( $r_0 = 1.115$  fm) for the  ${}^6\text{Li} + {}^{120}\text{Sn}$  ( ${}^7\text{Li} + {}^{119}\text{Sn}$ ) reaction. Such a range parameter is sufficient to consider all the dominant channel couplings during the fusion process in the EDWSP model. As the TF yields include the CF and ICF parts, therefore, the difference in the values of the range parameters in the EDWSP model for the CF and TF predictions directly measures the ICF contributions. As already mentioned, the loosely bound projectile breaks up into two parts via  ${}^6\text{Li} \rightarrow \alpha + d$  ( ${}^7\text{Li} \rightarrow \alpha + t$ ) and the probability of absorption of deuterium (tritium) for  ${}^6\text{Li}$  ( ${}^7\text{Li}$ ) by target is prominent; therefore, the presence of the  ${}^{120}\text{Sb}$  isotope as an ICF part further confirms the breakup of a loosely bound system in the force field of the target. Thus, the TF cross-section data are not inhibited with respect to the EDWSP predictions over the whole range of incident energies, as evident from Fig. 3. The similar behaviors of TF cross sections are also inferred from Ref. [24].

## 2. Fusion dynamics by using the $\ell$ -summed Wong model

It is well known that the low binding energy of  ${}^{6,7}\text{Li}$  nuclei gives rise to an incomplete fusion process. Hence, the discussion above further motivates us to account the fusion process via addressing complete and incomplete fusion processes. Since the EDWSP formalism alone could take care of CF and ICF processes independently in terms of range parameter ( $r_0$ ). Furthermore, to support and further concretize the EDWSP predictions, the  $\ell$ -summed Wong formula is used. Because the angular momentum plays the eminent role in deciding the fate of the compound nucleus formation, the constraints on the angular momentum  $\ell$  window enable us to distinguish between the CF, ICF, and TF processes.

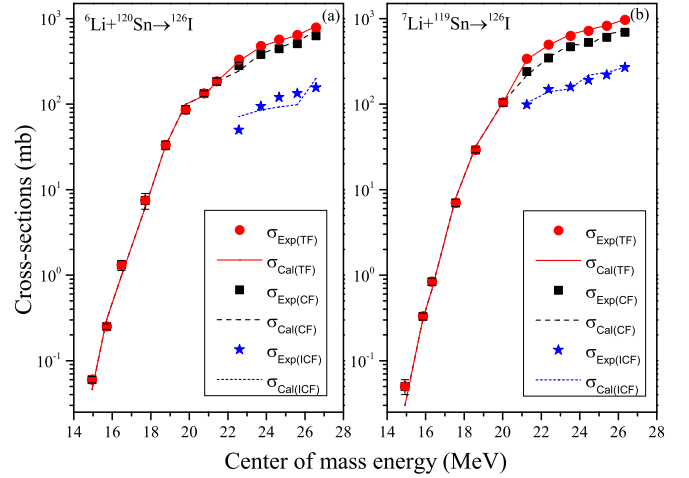


FIG. 5. Comparison of complete fusion (CF), total fusion (TF), and incomplete fusion cross section determined using the  $\ell$ -summed Wong formula for the  ${}^6\text{Li} + {}^{120}\text{Sn}$  and  ${}^7\text{Li} + {}^{119}\text{Sn}$  reactions. The calculated cross sections are compared with the available experimental data [24].

In case of the  $\ell$ -summed Wong formula, the  $\ell$  values are truncated up to  $\ell_{crit.}$  for the fusion process, above which the projectile nucleus is unable to fuse with the target nucleus. The critical  $\ell$  values are calculated from the sharp cutoff approximation [6]. For the total fusion cross section, which is the sum of CF and ICF, the  $\ell$  values are summed up to  $\ell_{max}$ . The angular momentum for ICF process is taken as  $\ell_{crit.} < \ell \leq \ell_{max}$ .

In Fig. 4(a) the angular-momentum distribution for the  ${}^6\text{Li} + {}^{120}\text{Sn}$  reaction at  $E_{c.m.} = 26$  MeV is shown, which clearly demonstrates the utility of the  $\ell$ -summed Wong model. Here,  $\ell_{crit.}$  for the  ${}^6\text{Li}$ -induced reaction is deduced as  $12\hbar$  while  $\ell_{max} = 13\hbar$ . The variation in  $\ell$  so obtained from  $\ell$ -summed Wong is analyzed for different energies, as shown in Fig. 4(b). The  $\ell_{crit.}$  (and  $\ell_{max}$ ) values increase with increasing energy. Using these values, the complete, incomplete, and total fusion cross sections are determined for the  ${}^6\text{Li} + {}^{120}\text{Sn}$  and  ${}^7\text{Li} + {}^{119}\text{Sn}$  reactions within the framework of the  $\ell$ -summed Wong model.

Figure 5 compares the fusion cross sections determined for the  ${}^6\text{Li} + {}^{120}\text{Sn}$  and  ${}^7\text{Li} + {}^{119}\text{Sn}$  reactions using the  $\ell$ -summed Wong formula, wherein the  $\ell_{crit.}$  and  $\ell_{max}$  values are calculated as discussed above. The result shows that the calculated CF, ICF, and TF cross sections are in good agreement with the available data. This implies that the  $\ell$ -summed Wong model is reasonably good in addressing the CF as well as the ICF processes. The observation of the CF and TF cross sections for  ${}^6\text{Li}$  is consistent with that of the  ${}^7\text{Li}$  case, showing decent agreement with the experimental data [24]. However, a small discrepancy in the ICF of  ${}^6\text{Li}$  and  ${}^7\text{Li}$  has been observed, which might arise due to the choice of  $\ell$ . Concluding, the overall comparison is fairly good for both the reaction channels in view of fusion.

After discussing the fusion analysis by using the EDWSP model and the  $\ell$ -summed Wong model, the decay study of compound nuclei formed using the CF and ICF channels of

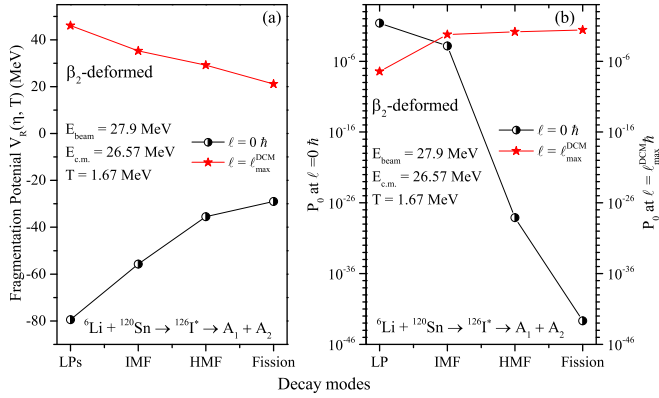


FIG. 6. Variation of (a) mass fragmentation, potential minimized in charge coordinate  $\eta_Z$  and (b) preformation probability  $P_0$  of different decay modes (LP, IMF, HMF, fission) of  $^{126}\text{I}^*$  compound nucleus at center-of-mass energy  $E_{c.m.} = 26.57$  MeV shown at extreme  $\ell$  values.

the given reactions is made using the DCM and presented in the preceding Sec. III B.

## B. Decay dynamics

Experimentally [24], the excitation functions (EFs) of CF and ICF decay products were measured for  $^6\text{Li} + ^{120}\text{Sn}$  and  $^7\text{Li} + ^{119}\text{Sn}$  reactions at energies ( $E_{c.m.} = 14.0\text{--}27.0$  MeV) around the Coulomb barrier. In the context of the available data [24], an attempt is made to study the relative population of different fragments in the decay of  $^{126}\text{I}^*$  (formed in both CF) and  $^{122}\text{Sb}^*$  (formed in both ICF). For the chosen compound systems, the relative cross sections of various LPs ( $A \leq 4, Z \leq 2$ ) is observed. Experimental observations [24] suggest that there is a predominant production of  $xn$  ( $x = 2, 3$  for CF and  $x = 2$  for ICF) exit channels in the decay of these compound nuclei. Therefore, a comparative analysis and thus the relative possibility of different  $xn$  channels is examined for both CF and ICF channels. To discuss the outcomes more effectively, this section is divided into two sections: Sec. III B 1 presents the decay of  $^{126}\text{I}$  formed in  $^6\text{Li} + ^{120}\text{Sn}$  and  $^7\text{Li} + ^{119}\text{Sn}$  reactions and Sec. III B 2 describes the dynamics of different exit fragments emitted in the decay of  $^{122}\text{Sb}$  formed in the ICF channel.

### 1. CF decay dynamics

The contribution of fragments participating in the decay channel of compound nuclei can be well understood through the variation of fragmentation potential and preformation probability. Figure 6 describes the mass fragmentation potential  $V_R(\eta, T)$ , minimized in charge or mass coordinate  $\eta_Z$ , and preformation probability  $P_0$  for the decay of  $^{126}\text{I}^*$  at extreme  $\ell$  values ( $\ell = 0\hbar$  and  $\ell = \ell_{\text{max}}^{\text{DCM}}$ ) for a fixed  $T = 1.67$  MeV. This value of  $T$  corresponds to the maximum center-of-mass energy  $E_{c.m.} = 26.57$  MeV. The main purpose to analyze the fragmentation behavior in Fig. 6(a) is to examine the potential for various mass regions such as ER, IMF, HMF, and fission so that the comparative dynamics of different decay modes can be determined. Furthermore, it is worthwhile to mention

that the lower fragmentation potential of the fragments leads to the higher probability for them to decay. Also, it is evident from the figure that, at minimum  $\ell$  value, ER has the lower magnitude of the fragmentation potential, which is reversed at higher  $\ell$  values. As a consequence, the variation of  $P_0$  in Fig. 6(b) clearly reveals that ERs are energetically more favorable in the lower- $\ell$ -value region. However, IMFs, HMFs, and fission fragments become dominant in the higher- $\ell$ -value region.

As mentioned earlier,  $xn$  ( $x = 2, 3$ ) exit channels are observed [24] to participate predominantly in the decay of  $^{126}\text{I}^*$  formed in the  $^6\text{Li} + ^{120}\text{Sn}$  and  $^7\text{Li} + ^{119}\text{Sn}$  reactions. Therefore, a comparative analysis of  $xn$  ( $x = 2, 3$ ) and other LPs [ $\neq xn$  ( $x = 2, 3$ )] participating in the decay of  $^{126}\text{I}^*$  CN is depicted in terms of their average preformation probability  $P_0^{\text{Avg.}}$  and average penetration or tunneling probability  $P^{\text{Avg.}}$  in Fig. 7 at  $E_{c.m.} = 26.57$  MeV. Here, it is important to mention that the upper panels of Fig. 7 i.e., Figs. 7(a)–7(c), display the results for the  $^6\text{Li} + ^{120}\text{Sn}$  reaction and the lower panels, i.e., Figs. 7(d)–7(f), exhibit the theoretical observations for the  $^7\text{Li} + ^{119}\text{Sn}$  reaction. Figures 7(a) and 7(d) display the variation of  $P_0^{\text{Avg.}}$  [based on  $V_R(\eta, T)$ ] as a function of  $\ell$  for the illustrative two groups of LPs for the given reactions. Interesting enough, the LPs [ $\neq xn$  ( $x = 2, 3$ )] competes with the  $xn$  ( $x = 2, 3$ ) neutron channels. Figures 7(a) and 7(d) illustrates the higher probability of the former case. However, this scenario is reversed in the case of the tunneling probability depicted in Figs. 7(b) and 7(e). Here,  $xn$  ( $x = 2, 3$ ) neutron channels dominates the other LPs in the decay channel and the difference in  $P^{\text{Avg.}}$  values of the illustrative groups of LPs actually takes precedence over the difference of their  $P_0^{\text{Avg.}}$  values. Consequently,  $xn$  ( $x = 2, 3$ ) neutron channels make the largest contribution to the ER cross section, which is distinctly apparent in Figs. 7(c) and 7(f). This figure reports the dominating nature of  $xn$  ( $x = 2, 3$ ) outgoing particles through the variation of average of product  $P_0P$  as a function of  $\ell$ . In other words, average  $P_0P$  values are higher for  $2n$  and  $3n$  neutron channels in comparison to other LP competing LP fragments.

In DCM, the cross sections are addressed by optimizing the neck-length parameter  $\Delta R$  and the DCM has the characteristic property of barrier lowering that is included via  $\Delta R$ . Figures 8(a) and 8(b) depicts the variation of neck-length parameter  $\Delta R$  and barrier modification  $\Delta V_B$ , respectively, with respect to the beam energy  $E_{\text{beam}}$  for both groups of outgoing LPs =  $2n, 3n$  and LPs  $\neq 2n, 3n$  in the decay of  $^{126}\text{I}^*$  formed in the  $^6\text{Li} + ^{120}\text{Sn}$  reaction. Here,  $\Delta R$  values are optimized in a way that major part of the decay cross sections should contribute to  $2n$  and  $3n$  emission, as suggested in the experimental data [24]. Furthermore,  $\Delta V_B$  is equivalent to the difference between the actual potential  $V(R_a)$  used for penetration and the top of the barrier  $V_B$ . This figure indicates a direct relation between  $\Delta R$  and  $\Delta V_B$ , the magnitude of the barrier modification ( $\Delta V_B$ ) decreases with the increase in  $\Delta R$ , and vice versa. The variation of the  $\Delta R$  for the decay cross sections is sensitive to the CN's mass, excitation energy, outgoing fragments, etc. Different  $\Delta R$  values for LPs =  $2n, 3n$  and LPs  $\neq 2n, 3n$  neutron channels depicted in Fig. 8(a) signifies that distinct barrier modification is

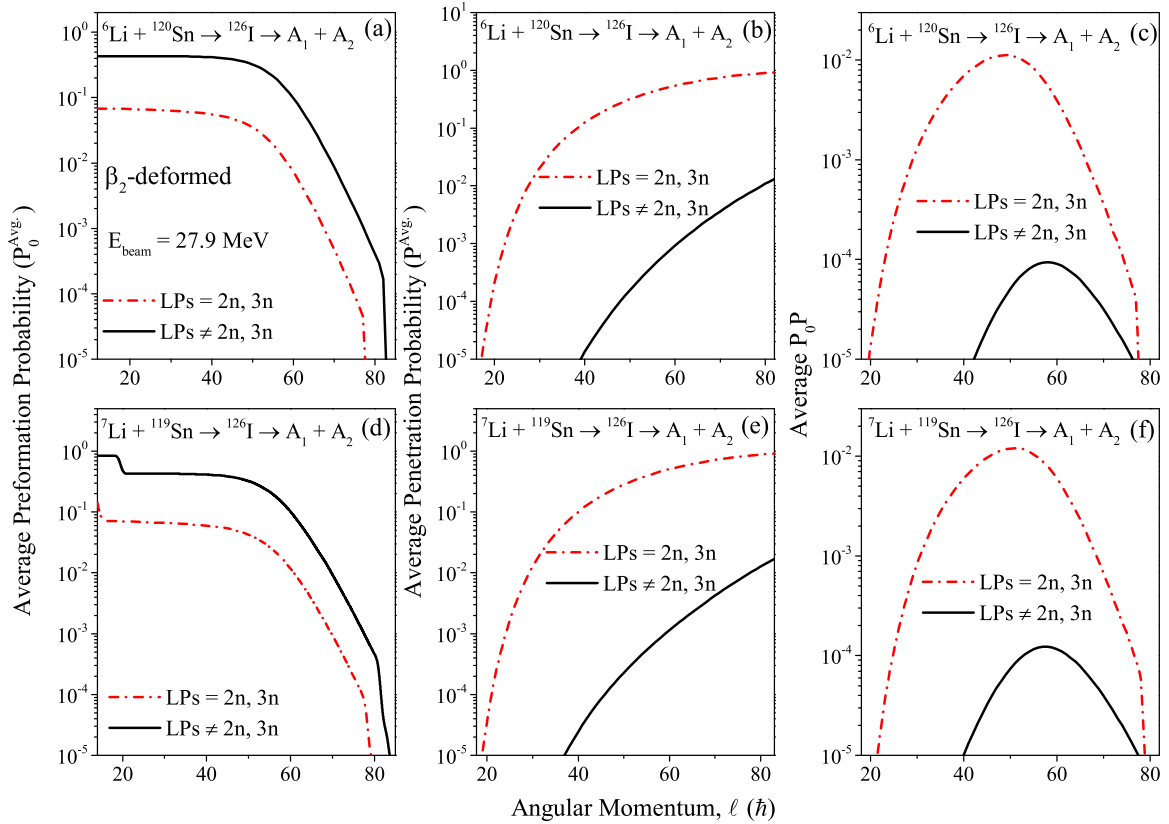


FIG. 7. Average of (a) preformation probability  $P_0^{\text{Avg.}}$  and (b) of penetrability  $P^{\text{Avg.}}$  and (c) the product  $P_0 P$  is plotted as a function of angular momentum for different evaporation channels of the  ${}^6\text{Li} + {}^{120}\text{Sn} \rightarrow {}^{126}\text{I}^*$  and  ${}^7\text{Li} + {}^{119}\text{Sn} \rightarrow {}^{126}\text{I}^*$  reactions at  $E_{\text{beam}} = 27.9$  MeV.

required for different neutron channels. Figure 8 clearly reports that the  $\Delta R$  values for LPs  $\neq 2n, 3n$  are lower than those for LPs  $= 2n, 3n$ . This implies that the first turning point  $R_a$  ( $=R_t + \Delta R$ ) is comparatively higher and thus closer to the barrier position  $R_B$  for LPs  $= 2n, 3n$ . As a consequence, the magnitude,  $|V(R_a) - V_B| = \Delta V_B$  diminishes, suggesting that

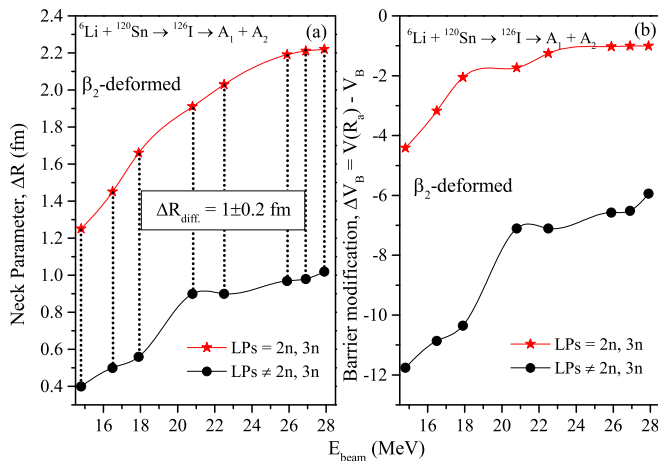


FIG. 8. (a) Variation of the neck-length parameter  $\Delta R$  obtained for the best fit to neutron fusion-evaporation data [24] and (b) barrier modification  $\Delta V_B$  as a function of beam energy  $E_{\text{beam}}$  for different  $xn$  emission channels of  ${}^6\text{Li} + {}^{120}\text{Sn} \rightarrow {}^{126}\text{I}^*$ .

lower barrier modification [shown in Fig. 8(b)] is required for  $xn$  ( $x = 2, 3$ ) neutron channels to participate in the decay of  ${}^{126}\text{I}^*$  CN. Furthermore, from Fig. 8(b), it is also observed that the magnitude of  $\Delta V_B$  (nonzero number at all energies) is highest at the lowest energy and decreases with increasing value of  $E_{\text{beam}}$  for all LPs. This implies that higher barrier modification is required at lower energies. Similar results are obtained for the  ${}^7\text{Li} + {}^{119}\text{Sn}$  reaction (not shown here to avoid repetition). Another important observation related to  $\Delta R$  values is noticed from the Table III that  $\Delta R$  for both  ${}^6\text{Li} + {}^{120}\text{Sn}$  and  ${}^7\text{Li} + {}^{119}\text{Sn}$  reactions are similar (or have a very minute difference  $\leq 0.03$  fm) at common given beam energies, e.g., at  $E_{\text{beam}} = 27.9$  MeV,  $\Delta R = 2.22$  fm for both aforementioned reactions, forming the same CN ( ${}^{126}\text{I}^*$ ). It is interesting to note here that this result is in line with the previous observation of DCM [75] for WBP-induced reactions forming the same compound nucleus at common energies.

The DCM-calculated cross sections (evaporation residue) for CF channels of both the reactions are compared with the experimental data [24] and the results are shown in Table III, it is clearly evident from Table III that the DCM-based ER cross sections are coherent with the available experimental data for both the reactions. Furthermore, a comparative analysis of DCM-based cross sections for the illustrated groups of  $xn$  ( $x = 2, 3$ ) neutron channels and other LPs [ $\neq xn$  ( $x = 2, 3$ )] is reported in Fig. 9. Figure clearly reveals that the  $xn$  ( $x = 2, 3$ ) neutron channels are the major contributor towards the decay cross sections of  ${}^{126}\text{I}^*$  CN formed in  ${}^6\text{Li} + {}^{120}\text{Sn}$  and

TABLE III. The DCM calculated and experimental neutron-evaporation residue cross sections for the decay of the  $^{126}\text{I}^*$  compound nucleus formed in WBP-induced  $^6\text{Li} + ^{120}\text{Sn}$  and  $^7\text{Li} + ^{119}\text{Sn}$  reactions compared with the experimental data [24]. The neck-length parameter, beam energies ( $E_{\text{beam}}$ ), and maximum angular momentum ( $\ell_{\text{max}}^{\text{DCM}}$ ) are also listed. The deformations are taken up to  $\beta_2$  with optimum orientations of outgoing fragments.

S. No.	$E_{\text{beam}}$ (MeV)	$E_{\text{c.m.}}$ (MeV)	$\ell_{\text{max}}^{\text{DCM}}$ ( $\hbar$ )	T (MeV)	$\Delta R$		$\sigma_{\text{DCM}}$		$\sigma_{\text{Total}}^{\text{DCM}}$ (mb)	$\sigma_{\text{Expt.}}$ (mb)
					LPs $\neq 2n, 3n$ (fm)	LPs = $2n, 3n$ (fm)	LPs $\neq 2n, 3n$ (mb)	LPs = $2n, 3n$ (mb)		
$^6\text{Li} + ^{120}\text{Sn} \rightarrow ^{126}\text{I}^*$										
1	14.8	14.09	78	1.37	0.40	1.25	0.001	0.005	0.006	$0.008 \pm 0.003$
2	16.5	15.71	82	1.42	0.50	1.45	0.015	0.222	0.237	$0.251 \pm 0.019$
3	17.9	17.05	84	1.45	0.56	1.66	0.057	2.609	2.666	$2.78 \pm 0.21$
4	20.8	19.81	94	1.52	0.90	1.91	3.60	77.88	81.46	$86.3 \pm 9.6$
5	22.5	21.43	95	1.56	0.90	2.03	5.282	170.48	170.47	$184 \pm 17$
6	25.9	24.67	96	1.63	0.97	2.19	10.599	424.66	435.23	$445 \pm 35$
7	26.9	25.62	96	1.65	0.98	2.21	11.150	494.77	505.90	$507 \pm 41$
8	27.9	26.57	96	1.67	1.02	2.22	16.113	565.41	581.53	$628 \pm 49$
$^7\text{Li} + ^{119}\text{Sn} \rightarrow ^{126}\text{I}^*$										
1	15.5	14.64	78	1.37	0.40	1.30	0.002	0.014	0.016	$0.02 \pm 0.01$
2	16.4	15.49	81	1.42	0.47	1.43	0.010	0.147	0.156	$0.15 \pm 0.02$
3	17.7	16.72	83	1.45	0.49	1.65	0.021	1.662	1.683	$1.74 \pm 0.13$
4	19.7	18.61	88	1.52	0.70	1.91	0.406	30.99	31.39	$29 \pm 2$
5	22.5	21.25	95	1.56	0.93	2.04	8.103	215.53	223.63	$240 \pm 21$
6	25.9	24.46	96	1.63	1.00	2.20	15.30	506.0	522.00	$526 \pm 4$
7	26.9	25.41	96	1.65	1.01	2.22	16.24	550.75	566.99	$602 \pm 49$
8	27.9	26.35	96	1.67	1.05	2.22	24.92	615.24	640.17	$692 \pm 56$

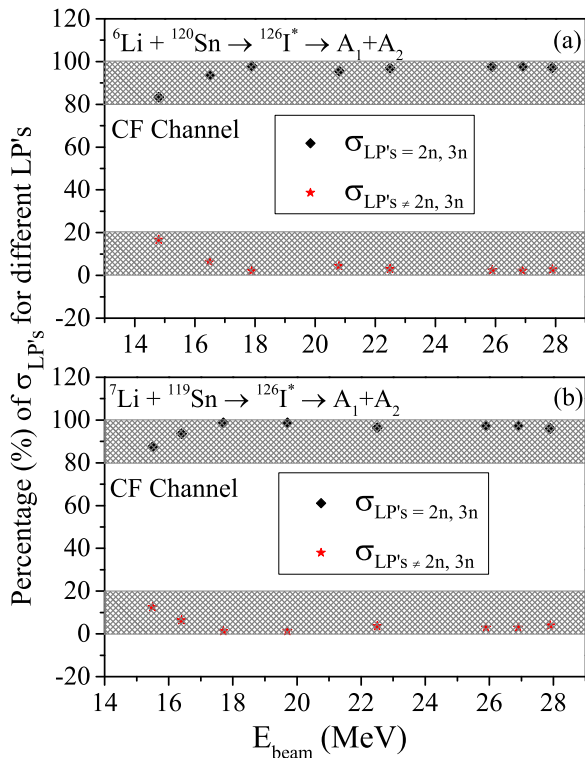


FIG. 9. Relative contribution of illustrated groups of  $xn$  ( $x = 2, 3$ ) neutron evaporation and other LPs [ $\neq xn$  ( $x = 2, 3$ )] in the exit channel of the (a)  $^6\text{Li} + ^{120}\text{Sn} \rightarrow ^{126}\text{I}^*$  and (b)  $^7\text{Li} + ^{119}\text{Sn} \rightarrow ^{126}\text{I}^*$  reactions as a function of beam energy ( $E_{\text{beam}} = 14.8\text{--}27.9$  MeV).

$^7\text{Li} + ^{119}\text{Sn}$  reactions. At most of the energies, the percentage of  $\sigma_{LPs=2n,3n} \geq 90\%$ .

## 2. Incomplete-fusion decay dynamics

In this section, the dynamics of fragments in the decay of CN formed in ICF channels of chosen reactions is discussed for beam energies ( $E_{\text{beam}} \approx 21.4\text{--}27.9$  MeV) in reference to the experimental data [24]. The beam energies of WBPs in  $^6\text{Li} + ^{120}\text{Sn}$  and  $^7\text{Li} + ^{119}\text{Sn}$  reactions are further corrected for ICF according to Eq. (24), so one can extract the appropriate beam energy for the requisite ICF channel. As mentioned earlier, according to the experimental evidence [24], there is a possibility of fusion of deuterium (in the ICF channel of  $^6\text{Li} + ^{120}\text{Sn}$ ) and tritium (in the ICF channel of  $^7\text{Li} + ^{119}\text{Sn}$ ) with respective targets followed by the  $2n$  emission to produce  $^{120}\text{Sb}$  in the decay of the  $^2\text{H} + ^{120}\text{Sn} \rightarrow ^{122}\text{Sb}^*$  and  $^3\text{H} + ^{119}\text{Sn} \rightarrow ^{122}\text{Sb}^*$  ICF channels. To investigate the relative contribution of particle emission in both reactions, the preformation probability  $P_0^{LPs}$  for LPs is plotted as a function of angular momentum  $\ell$  in Fig. 10 for both ICF reactions at two beam energies ( $E_{\text{beam}} = 22.5$  and  $27.9$  MeV). This figure suggests that the  $P_0^{LPs}$  for both ICF channels is almost same at lower  $\ell$  values. However, a significant shift is seen in the magnitude of  $P_0^{LPs}$  at higher  $\ell$  values, showing the clear prominence of the  $^3\text{H} + ^{119}\text{Sn} \rightarrow ^{122}\text{Sb}^*$  channel. Furthermore, comparing Figs. 10(a) and 10(b), one can observe that the difference of  $P_0^{LPs}$  values for given ICF channels diminishes with increasing energy.

Next, Fig. 11 displaying the analog behavior of  $\Delta R$  and  $\Delta V_B$  (for  $^2\text{H} + ^{120}\text{Sn} \rightarrow ^{122}\text{Sb}^*$ ) as a function of  $E_{\text{beam}}$  for

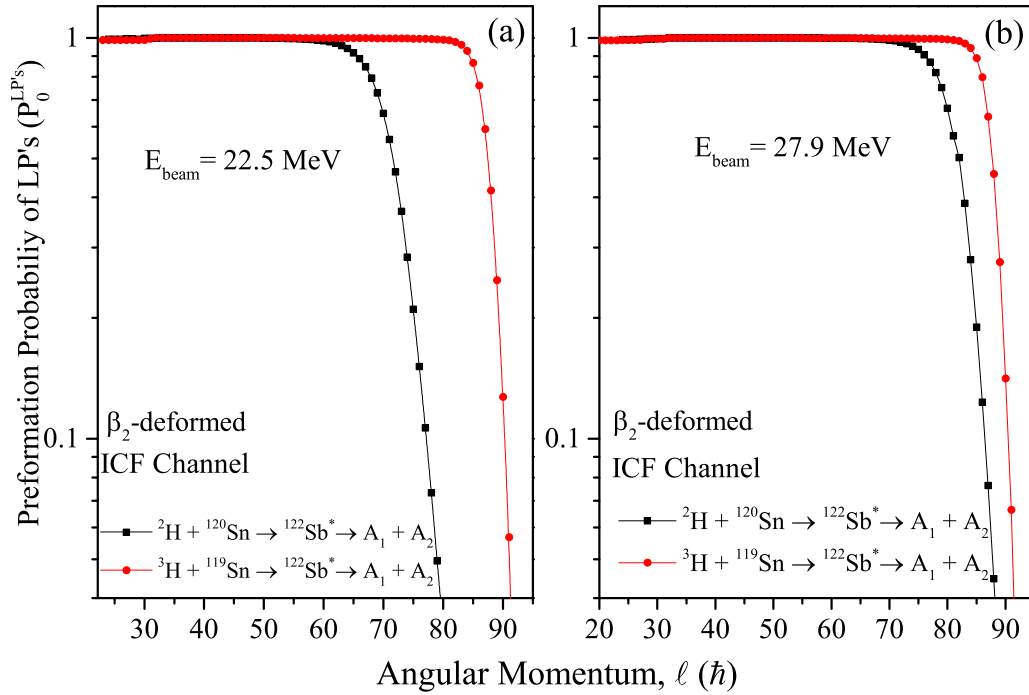


FIG. 10. Variation of the preformation probability  $P_0^{LPs}$  as a function of angular momentum for the emission of light particles in the decay of  $^{122}\text{Sb}^*$  formed in  $^2\text{H} + ^{120}\text{Sn}$  and  $^3\text{H} + ^{119}\text{Sn}$  ICF channels of given reactions induced by WBPs  $^6\text{Li}$  and  $^7\text{Li}$ , respectively, at  $E_{\text{beam}} = 27.9$  MeV.

LPs =  $2n$  and  $\neq 2n$  shows a pattern similar to the one observed in CF decays for LPs =  $2n$  and LPs  $\neq 2n, 3n$ . Furthermore, in the case of ICF,  $\Delta R$  is tuned to obtain the maximum possible contribution of the  $2n$  emission, as indicated by the experimental data [24]. Figure 11 clearly suggest that the LPs  $\neq 2n$  demands higher barrier modification (higher magnitude  $|\Delta V_B|$ ) owing to the lesser value of  $\Delta R$ , which in turn reduces their tunneling probability shown in Fig. 12(a). Furthermore, to illustrate the reliance of tunneling or penetration probability

on barrier modification, variation of  $|\Delta V_B|$  as a function of  $\ell$  is depicted in Fig. 12(b). This figure clearly reveals that  $P$  of the particles directly depends on the their barrier modification. A higher value of  $|\Delta V_B|$  for  $2n$  emission in Fig. 12(b) leads to the higher value of their  $P$  in Fig. 12(a). Similar behavior is noticed for the  $^3\text{H} + ^{119}\text{Sn} \rightarrow ^{122}\text{Sb}^*$  ICF channel (not shown here to avoid repetition).

The DCM-calculated ICF cross sections (shown in Table IV) are in coherence with the available data [24]. Furthermore, the relative analysis of the percent contribution

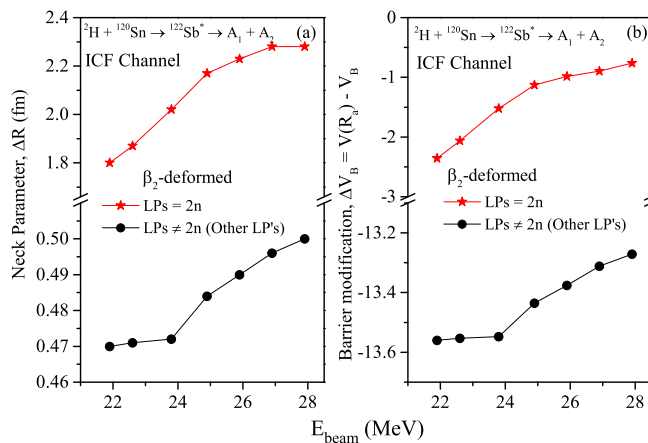


FIG. 11. (a) Variation of the neck-length parameter  $\Delta R$  obtained from the best fit to neutron fusion-evaporation data [24] and (b) barrier modification  $\Delta V_B$  as a function of beam energy  $E_{\text{beam}}$  for different  $xn$  emission channels of  $^2\text{H} + ^{120}\text{Sn}$  ICF channel of the  $^6\text{Li} + ^{120}\text{Sn} \rightarrow ^{126}\text{I}^*$  reaction.

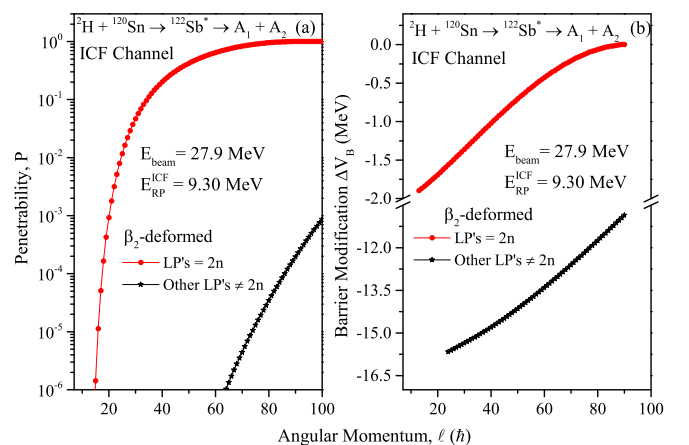


FIG. 12. (a) Variation of penetrability  $P$  and (b) barrier modification  $\Delta V_B$  as a function of angular momentum  $\ell$  for different  $xn$  emission channels of  $^2\text{H} + ^{120}\text{Sn}$  ICF channel of  $^6\text{Li} + ^{120}\text{Sn} \rightarrow ^{126}\text{I}^*$  reaction.

TABLE IV. The DCM calculated and experimental neutron-evaporation residue cross sections for the decay of  $^{122}\text{Sb}^*$  compound nucleus formed in  $^2\text{H} + ^{120}\text{Sn}$  and  $^3\text{H} + ^{119}\text{Sn}$  ICF channels compared with the experimental data [24]. The neck-length parameter, beam energies ( $E_{\text{beam}}$ ), and Remnant Projectile energies ( $E_{RP}^{\text{ICF}}$ ) for ICF are also listed. The maximum angular-momentum value for both ICF reactions is  $\ell_{\text{max}}^{\text{DCM}} \approx 90\hbar$ . The deformations are taken up to  $\beta_2$  with optimum orientations of outgoing fragments.

S. No.	$E_{\text{beam}}$ (MeV)	$E_{RP}^{\text{ICF}}$ (MeV)	T (MeV)	$\Delta R$		$\sigma_{\text{DCM}}$		$\sigma_{\text{Total}}^{\text{DCM}}$ (mb)	$\sigma_{\text{Expt.}}$ (mb)
				LPs $\neq 2n, 3n$ (fm)	LPs = $2n, 3n$ (fm)	LPs $\neq 2n, 3n$ (mb)	LPs = $2n, 3n$ (mb)		
$^2\text{H} + ^{120}\text{Sn} \rightarrow ^{122}\text{Sb}^*$									
1	21.4	7.10	1.181	0.467	1.74	0.69	12.72	13.41	$14.9 \pm 1.6$
2	21.8	7.27	1.186	0.470	1.80	0.90	21.50	22.40	$20.5 \pm 2.2$
3	22.5	7.50	1.193	0.471	1.87	0.94	29.03	29.97	$31.9 \pm 3.1$
4	23.7	7.90	1.206	0.472	2.02	1.02	49.59	50.61	$49.9 \pm 4.6$
5	24.9	8.30	1.218	0.484	2.17	2.76	93.20	95.96	$94.3 \pm 8.8$
6	25.9	8.64	1.228	0.490	2.23	4.24	113.12	117.36	$120 \pm 11$
7	26.9	8.97	1.238	0.496	2.28	4.601	120.16	124.76	$134 \pm 13$
8	27.9	9.30	1.248	0.500	2.35	5.520	140.61	146.130	$156 \pm 14$
$^3\text{H} + ^{119}\text{Sn} \rightarrow ^{122}\text{Sb}^*$									
1	22.5	9.64	1.341	0.550	2.09	11.66	93.61	105.27	$98 \pm 8.9$
2	23.7	10.16	1.355	0.630	2.17	26.67	111.90	138.57	$149 \pm 13$
3	24.9	10.67	1.369	0.660	2.22	31.14	125.25	156.39	$159 \pm 15$
4	25.9	11.10	1.381	0.690	2.33	32.27	155.21	194.48	$191 \pm 17$
5	26.9	11.53	1.392	0.701	2.35	41.70	158.00	199.46	$219 \pm 20$
6	27.9	11.96	1.404	0.710	2.35	44.60	214.96	259.57	$268 \pm 25$

of  $2n$  and other LPs towards the decay cross sections of  $^{122}\text{Sb}^*$  is reported in Table IV for both the  $^2\text{H} + ^{120}\text{Sn} \rightarrow ^{122}\text{Sb}^*$  and  $^3\text{H} + ^{119}\text{Sn} \rightarrow ^{122}\text{Sb}^*$  ICF reactions. Table IV clearly illustrates that the major contribution towards ER of given reactions is from  $2n$  with  $\sigma_{2n} \geq 80\%$  for both reactions. Lastly, Fig. 13 illustrates the variations of neck-parameter values ( $\Delta R$ ) with respect to temperature based on the optimal fitting of neutron fusion-evaporation data [24] for both the CF and ICF channels of the  $^6\text{Li} + ^{120}\text{Sn}$  and  $^7\text{Li} + ^{119}\text{Sn}$  reactions. The figure clearly demonstrates that the neck-parameter values monotonically increase with temperature. Additionally, it is noteworthy that the  $\Delta R$  values are consistently higher

for the  $2n$  and  $3n$  channels as compared with other channels, primarily due to their major contribution in the decay modes of the reactions under consideration.

#### IV. SUMMARY

The theoretical estimations of the CF cross sections at above-barrier energies obtained using the EDWSP model predict a fusion suppression factor of the order 18% (5%) for the  $^6\text{Li} + ^{120}\text{Sn}$  ( $^7\text{Li} + ^{119}\text{Sn}$ ) reaction while the same calculations reasonably addressed the CF cross-section data at below-barrier energies. The EDWSP based suppression factors are significantly lower than the values reported in the literature. The EDWSP based calculations fairly reproduce the CF data at below-barrier energies, whereas a reduction factor of 18% (5%) is needed to explain above-barrier CF data of the  $^6\text{Li} + ^{120}\text{Sn}$  ( $^7\text{Li} + ^{119}\text{Sn}$ ) reaction. Therefore, the effect of the breakup channel is correlated with the breakup threshold of the loosely bound system. The smaller breakup threshold for a lighter projectile ( $^6\text{Li}$ ) in comparison with that of a heavier projectile ( $^7\text{Li}$ ) gives higher suppression effects at energies lying above the Coulomb barrier.

Total fusion (TF) cross-section data, which is sum of complete fusion (CF) and incomplete fusion (ICF), is not expected to be suppressed when compared with the predictions of EDWSP model. In this model, the range parameter  $r_0 = 1.120$  fm ( $r_0 = 1.115$  fm) fairly addresses the TF cross-section data of the  $^6\text{Li} + ^{120}\text{Sn}$  ( $^7\text{Li} + ^{119}\text{Sn}$ ) reaction, whereas the range parameter  $r_0 = 1.090$  fm ( $r_0 = 1.080$  fm) is required to explain the behavior of the CF cross-section data of the  $^6\text{Li} + ^{120}\text{Sn}$  ( $^7\text{Li} + ^{119}\text{Sn}$ ) reactions. Furthermore, the difference in the value of the range parameter  $r_0$  for the CF and TF cross-section data for the given reaction identifies the

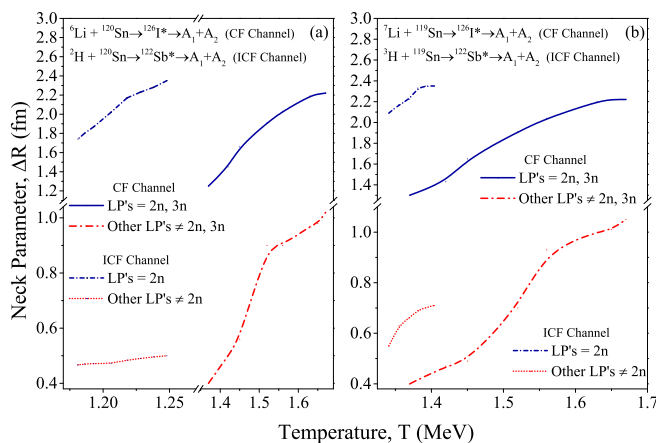


FIG. 13. Variation of the neck-length parameter ( $\Delta R$ ) obtained for the best fit to neutron fusion-evaporation data [24] as a function of temperature  $T$  for different CF and ICF channels of the given reactions [24].

ICF contribution in the fusion process. The ICF component is deficit of the loss of flux going to the CF channel. As the probability of absorption of deuteron  $d$  and tritium in the  ${}^6\text{Li} + {}^{120}\text{Sn}$  ( ${}^7\text{Li} + {}^{119}\text{Sn}$ ) reaction is prominent and thus remits in the ICF yields as Sb isotopes.

Furthermore, fusion studies based on the  $\ell$ -summed Wong formula provides relevant information associated with the angular-momentum distribution of the compound nucleus. It is observed that  $\ell_{\text{crit}}$  (and  $\ell_{\text{max}}$  values) calculated using sharp cutoff approximation increase with increasing energy for both the  ${}^6\text{Li}$ - and  ${}^7\text{Li}$ -induced reactions. The systematic investigation carried out for the given reactions provide reasonable agreement of theoretical observation with the experimental data.

Apart from the fusion, the decay dynamics of the  ${}^6\text{Li} + {}^{120}\text{Sn}$  and  ${}^7\text{Li} + {}^{119}\text{Sn}$  reaction is investigated by using the DCM formalism. Owing to the weakly bound nature of projectiles ( ${}^{6,7}\text{Li}$ ), both complete and incomplete fusion analysis is worked out. A comparative analysis of different decay modes (LPs, IMF, HMF, and fission) is examined within the DCM framework. The decay paths of both CF and ICF are examined using various components such as fragmentation potential, preformation probability, barrier height, barrier modification, etc. Furthermore, the neutron evaporation residue cross sections are attained for both CF and ICF channels. Furthermore, the neck-length parameter and barrier modification show analogous behavior as a function of beam energy. This suggest that the lower neck value corresponds to higher barrier modification for both CF and ICF decay paths. Also,  $\Delta R$  values for both reactions are found to be identical at common given beam energies. Furthermore, a

comparative analysis of LPs emission in the decay of  ${}^{122}\text{Sb}^*$  formed in  ${}^2\text{H} + {}^{120}\text{Sn}$  (WBP:  ${}^6\text{Li}$ ) and  ${}^3\text{H} + {}^{119}\text{Sn}$  (WBP:  ${}^7\text{Li}$ ) ICF channels suggest that LPs emission is predominate in the  ${}^3\text{H} + {}^{119}\text{Sn}$  ICF reaction. Finally, the relative contribution of different  $xn$  neutron evaporation channels is estimated for both CF and ICF decays. It is observed that  $xn$  ( $x = 2, 3$ ) govern the CF decay with  $\sigma_{LPs=2n,3n} \geq 90\%$  and, for ICF,  $2n$  emission is perceived as the major contributor in the exit channel with  $\sigma_{2n} \geq 80\%$  for both the reactions. Also, the neck-parameter values of all decay modes increases with increase in temperature and are consistently larger for dominant neutron evaporation channels, i.e., LPs =  $2n, 3n$  for CF and LPs =  $2n$  for ICF.

In view of the analysis made using three mathematical approaches, it is observed that the  $\ell$ -summed Wong formula helps in differentiating the angular-momentum transfer in the CF and ICF processes. However, the EDWSP model separates CF and ICF data using the range parameter  $r_0$  and the diffuseness of the EDWSP model. Finally, the DCM provides the structural information of decay channels of compound nuclei formed in the CF and ICF channels of the  ${}^6\text{Li} + {}^{120}\text{Sn}$  and  ${}^7\text{Li} + {}^{119}\text{Sn}$  reactions.

#### ACKNOWLEDGMENTS

The financial support from the Indian Institute of Technology, Ropar in the form of Post-Doctoral Fellowship to Neha Grover is gratefully acknowledged. M.K.S. acknowledges the financial support by the Science Engineering Research Board (SERB), Department of Science and Technology (DST), Govt. of India, File No. CRG/2021/001144.

- 
- [1] C. S. Palshetkar *et al.*, *Phys. Rev. C* **89**, 024607 (2014).  
 [2] A. M. Moro and J. Lei, *Few-Body Syst.* **57**, 319 (2016).  
 [3] Y. E. Penionzhkevich, *J. Phys.: Conf. Ser.* **420**, 012068 (2013).  
 [4] K. J. Cook, E. C. Simpson, L. T. Bezzina, M. Dasgupta, D. J. Hinde, K. Banerjee, A. C. Berriman, and C. Sengupta, *Phys. Rev. Lett.* **122**, 102501 (2019).  
 [5] J. Wilczyński, *Nucl. Phys. A* **216**, 386 (1973).  
 [6] M. Gull, K. Kumar, S. Ali, T. Ahmad, S. Dutt, I. A. Rizvi, A. Agarwal, and R. Kumar, *Phys. Rev. C* **98**, 034603 (2018).  
 [7] A. Diaz-Torres, *J. Phys. G* **37**, 075109 (2010).  
 [8] H. C. Britt and A. R. Quinon, *Phys. Rev.* **124**, 877 (1961).  
 [9] K. Hagino, M. Dasgupta, and D. J. Hinde, *Nucl. Phys. A* **738**, 475 (2004).  
 [10] A. Diaz-Torres, D. J. Hinde, J. A. Tostevin, M. Dasgupta, and L. R. Gasques, *Phys. Rev. Lett.* **98**, 152701 (2007).  
 [11] A. Diaz-Torres, *Comput. Phys. Commun.* **182**, 1100 (2011).  
 [12] J. Rangel, M. R. Cortes, J. Lubian, and L. F. Canto, *Phys. Lett. B* **803**, 135337 (2020).  
 [13] H. Tricoire, C. Gerschel, A. Gillibert, and N. Perrin, *Z. Phys. A* **323**, 163 (1986).  
 [14] A. S. Umar, M. R. Strayer, D. J. Ernst, K. R. Sandhya Devi, *Phys. Rev. C* **30**, 1934 (1984).  
 [15] H. Kruse, B. V. Jacak, J. J. Molitoris, G. D. Westfall, and H. Stöcker, *Phys. Rev. C* **31**, 1770 (1985).  
 [16] T. C. Awes, G. Poggi, C. K. Gelbke, B. B. Back, B. G. Glagola, H. Breuer, and V. E. Viola, Jr., *Phys. Rev. C* **24**, 89 (1981).  
 [17] M. Blann, *Phys. Rev. C* **31**, 1245 (1985).  
 [18] R. Serber, *Phys. Rev.* **72**, 1008 (1947).  
 [19] N. Austern, Y. Iseri, M. Kamimura, M. Kawai, G. Rawitscher, and M. Yahiro, *Phys. Rep.* **154**, 125 (1987).  
 [20] A. M. Moro, *Phys. Rev. C* **92**, 044605 (2015).  
 [21] G. Potel, G. Perdikakis, B. V. Carlson, M. C. Atkinson *et al.*, *Eur. Phys. J. A* **53**, 178 (2017).  
 [22] B. V. Carlson, T. Frederico, and M. S. Hussein, *Phys. Lett. B* **767**, 53 (2017).  
 [23] V. Jha, V. V. Parkar, and S. Kailas, *Phys. Rep.* **845**, 1 (2020).  
 [24] M. Fisichella, A. C. Shotton, P. Figuera, J. Lubian *et al.*, *Phys. Rev. C* **95**, 034617 (2017).  
 [25] M. Singh, S. S. Duhan, and R. Kharab, *Mod. Phys. Lett. A* **26**, 2129 (2011).  
 [26] M. Singh, Sukhvinder, and R. Kharab, *Nucl. Phys. A* **897**, 179 (2013).  
 [27] M. Singh, Sukhvinder, and R. Kharab, *Nucl. Phys. A* **897**, 198 (2013).  
 [28] M. S. Gautam, *Phys. Rev. C* **90**, 024620 (2014).  
 [29] M. S. Gautam, *Nucl. Phys. A* **933**, 272 (2015).  
 [30] M. S. Gautam, *Mod. Phys. Lett. A* **30**, 1550013 (2015).  
 [31] M. S. Gautam, *Phys. Scr.* **90**, 025301 (2015).  
 [32] M. S. Gautam, *Phys. Scr.* **90**, 055301 (2015).

- [33] M. S. Gautam, K. Vinod, and H. Kumar, *Chin. J. Phys.* **54**, 515 (2016).
- [34] M. S. Gautam, K. Vinod, and H. Kumar, *Braz. J. Phys.* **47**, 461 (2017).
- [35] M. S. Gautam, K. Vinod, and H. Khatri, *Eur. Phys. J. A* **53**, 212 (2017).
- [36] M. S. Gautam, H. Khatri, and K. Vinod, *Int. J. Mod. Phys. E* **28**, 1950006 (2019).
- [37] M. S. Gautam, H. Khatri, and K. Vinod, *Nucl. Phys. A* **984**, 9 (2019).
- [38] M. S. Gautam, S. Duhan, R. P. Chahal, H. Khatri, S. B. Kuhar, and K. Vinod, *Phys. Rev. C* **102**, 014614 (2020).
- [39] R. Kumar, M. Bansal, S. K. Arun, and R. K. Gupta, *Phys. Rev. C* **80**, 034618 (2009).
- [40] R. Kumar, M. K. Sharma, and R. K. Gupta, *Nucl. Phys. A* **870-871**, 42 (2011).
- [41] I. Sharma, R. Kumar, and M. K. Sharma, *Eur. Phys. J. A* **53**, 140 (2017).
- [42] I. Sharma, M. S. Gautam and M. K. Sharma, *Int. J. Mod. Phys. E* **26**, 1750077 (2017).
- [43] N. Grover, G. Kaur, and M. K. Sharma, *Phys. Rev. C* **93**, 014603 (2016).
- [44] G. Kaur, K. Sandhu, and M. K. Sharma, *Phys. Rev. C* **94**, 014615 (2016).
- [45] A. Kaur, G. Kaur, and M. K. Sharma, *Nucl. Phys. A* **941**, 152 (2015).
- [46] G. Sawhney, A. Kaur, M. K. Sharma, and R. K. Gupta, *Phys. Rev. C* **92**, 064303 (2015).
- [47] G. Kaur and M. K. Sharma, *Phys. Rev. C* **87**, 044601 (2013).
- [48] G. Kaur and M. K. Sharma, *Nucl. Phys. A* **884-885**, 36 (2012).
- [49] G. Sawhney, G. Kaur, M. K. Sharma, and R. K. Gupta, *Phys. Rev. C* **88**, 034603 (2013).
- [50] Rajni, R. Kumar, and M. K. Sharma, *Phys. Rev. C* **90**, 024315 (2014).
- [51] M. Kaur and M. K. Sharma, *Eur. Phys. J. A* **50**, 61 (2014).
- [52] H. J. Fink, J. Maruhn, W. Scheid, and, W. Greiner, *Eur. Phys. J. A* **268**, 321 (1974).
- [53] J. Maruhn and W. Greiner, *Phys. Rev. Lett.* **32**, 548 (1974).
- [54] B. B. Singh, M. K. Sharma, and R. K. Gupta, *Phys. Rev. C* **77**, 054613 (2008).
- [55] M. Dasgupta *et al.*, *Phys. Rev. C* **70**, 024606 (2004).
- [56] L. F. Canto, P. R. S. Gomes, R. Donangelo, and M. S. Hussein, *Phys. Rep.* **424**, 1 (2006).
- [57] D. L. Hill and J. A. Wheeler, *Phys. Rev.* **89**, 1102 (1953).
- [58] C. Y. Wong, *Phys. Rev. Lett.* **31**, 766 (1973).
- [59] L. C. Chamon *et al.*, *Phys. Rev. C* **66**, 014610 (2002).
- [60] K. Washiyama and D. Lacroix, *Phys. Rev. C* **78**, 024610 (2008).
- [61] C. Simenel, M. Dasgupta, D. J. Hinde, and E. Williams, *Phys. Rev. C* **88**, 064604 (2013).
- [62] A. S. Umar, C. Simenel, and V. E. Oberacker, *Phys. Rev. C* **89**, 034611 (2014).
- [63] A. B. Balantekin and N. Takigawa, *Rev. Mod. Phys.* **70**, 77 (1998).
- [64] K. Hagino, N. Rowley, and A. T. Kruppa, *Comput. Phys. Commun.* **123**, 143 (1999).
- [65] K. Hagino and N. Takigawa, *Prog. Theor. Phys.* **128**, 1061 (2012).
- [66] G. Royer and J. Mignen, *J. Phys. G* **18**, 1781 (1992).
- [67] M. Shuaib *et al.*, *Phys. Rev. C* **98**, 014605 (2018).
- [68] H. Kröger and W. Scheid, *J. Phys. G: Nucl. Phys.* **6**, L85 (1980).
- [69] N. J. Davidson, S. S. Hsiao, J. Markram, H. G. Miller, and Y. Tzeng, *Nucl. Phys. A* **570**, 61 (1994).
- [70] R. K. Gupta, R. Kumar, N. K. Dhiman, M. Balasubramaniam, W. Scheid, and C. Beck, *Phys. Rev. C* **68**, 014610 (2003).
- [71] G. Audi, A. H. Wapstra and C. Thiboult, *Nucl. Phys. A* **729**, 337 (2003); G. Audi and A. H. Wapstra, *ibid.* **595**, 409 (1995).
- [72] W. Myers and W. J. Swiatecki, *Nucl. Phys.* **81**, 1 (1966).
- [73] R. K. Gupta, in *Proceedings of the 5th International Conference on Nuclear Reaction Mechanisms, Varenna*, edited by E. Gadioli (Ricerca Scientifica ed Educazione Permanente, Milano, 1988), p. 416.
- [74] S. S. Malik and R. K. Gupta, *Phys. Rev. C* **39**, 1992 (1989).
- [75] M. Kaur, BirBikram Singh, M. K. Sharma, and R. K. Gupta, *Phys. Rev. C* **92**, 024623 (2015).